

A floating modular cover for high temperature open-tank molten salt solar-thermal volumetric receivers[☆]

Melanie Tetreault-Friend^{a,*}, Miguel Diago^b, Thomas A. Cooper^c, Luke A. Gray^d,
Alexander H. Slocum^d

^a Department of Mechanical Engineering, McGill University, 817 Sherbrooke West, H3A 0C3 Montreal, Quebec, Canada

^b Department of Mechanical and Materials Engineering, Khalifa University of Science and Technology, Masdar Institute, Masdar City, PO Box 54224, Abu Dhabi, United Arab Emirates

^c Department of Mechanical Engineering, York University, 11 Arboretum Lane, M3J 2S5 North York, Ontario, Canada

^d Department of Mechanical Engineering, Massachusetts Institute of Technology, 77 Massachusetts Avenue, Cambridge, MA 02139, USA

ARTICLE INFO

Keywords:

Concentrating solar power
Molten salt
Volumetrically absorbing receiver
Optically transparent thermal insulation

ABSTRACT

Directly irradiated and volumetrically absorbing liquid-based solar receivers promise to enhance peak solar flux limits relative to surface absorbers and enable simpler receiver designs with integral thermal storage. However, their thermal efficiency is limited by large thermal losses at high operating temperatures. The harsh, high temperature ($> 400\text{ °C}$) environments in liquid-based receivers impose significant material and system design constraints in mitigating heat losses, particularly for large-scale, commercial-size receivers. Here we report a new cover design that reduces thermal losses up to 51% while reducing the optical efficiency by less than 5%. The proposed design consists of floating hollow fused silica spheres and is stable in harsh high temperature environments, highly solar-transparent, reduces convective and radiative losses, and minimizes the surface area available for evaporation losses. In addition, the modular components allow easy online maintenance and unlike a single continuous window-pane, there is no limit to the surface size the spheres can cover. This transparent, insulating cover has the potential to enable much higher solar-thermal volumetric receiver temperatures and could also be used in other high temperature open bath industrial applications to provide energy savings.

1. Introduction

Concentrating Solar Power (CSP) technologies are a viable option to displace the use of fossil fuels in thermal energy systems, however their current energy production cost is comparatively high (Pacheco, 2001; Romero et al., 2002; U.S. Energy Information Administration, 2016). Increasing operating temperatures leads to higher heat engine efficiencies, which in turn reduces the Levelized Cost of Electricity (LCOE). However, the benefits of operating at higher temperatures are often offset by significant thermal losses, particularly for relatively low solar concentration ratios ($C < 500$) (Weinstein et al., 2015), and many methods have been explored to mitigate these losses in solar-thermal applications (Arpin et al., 2013; Cui et al., 2013; Reynolds et al., 2004; Rowe, 1981; Selvakumar and Barshilia, 2012; Singh et al., 2010; Weinstein et al., 2014). In particular, spectrally selective surface absorbers are engineered to maximize solar absorptivity and minimize thermal radiative losses (Atkinson et al., 2015; Bogaerts and Lampert,

1983; Kennedy, 2002). Surface absorbers readily convert solar irradiation into heat, however this heat must then be transferred to a working fluid, meaning the absorber must operate at a higher temperature than the fluid itself, resulting in higher surface heat losses (Fend et al., 2004; Kribus et al., 1999; Lenert and Wang, 2012). In liquid-based, direct absorption volumetric receivers, concentrated sunlight is beamed directly into a semi-transparent absorbing fluid (e.g. a nanofluid (Lenert and Wang, 2012; Ni et al., 2015; Otonicar et al., 2009) or molten salt (Drotning, 1978; Epstein et al., 1999; Slocum et al., 2011)), producing a more uniform fluid temperature. The temperatures at the surface associated with emissive losses are therefore expected to decrease relative to the bulk, which in turn leads to an increase in overall thermal efficiency (Khullar et al., 2014; Lenert and Wang, 2012; Ni et al., 2015). Nevertheless, high temperature open-top liquid-based receivers have large radiative and convective losses. In particular, the Concentrated Solar Power on Demand (CSPonD) concept (Slocum et al., 2011) illustrated in Fig. 1 is a system which consists of a

[☆] Dedicated to the memory of Dr. Thomas McKrell.

* Corresponding author.

E-mail address: melanie.tetreault-friend@mcgill.ca (M. Tetreault-Friend).

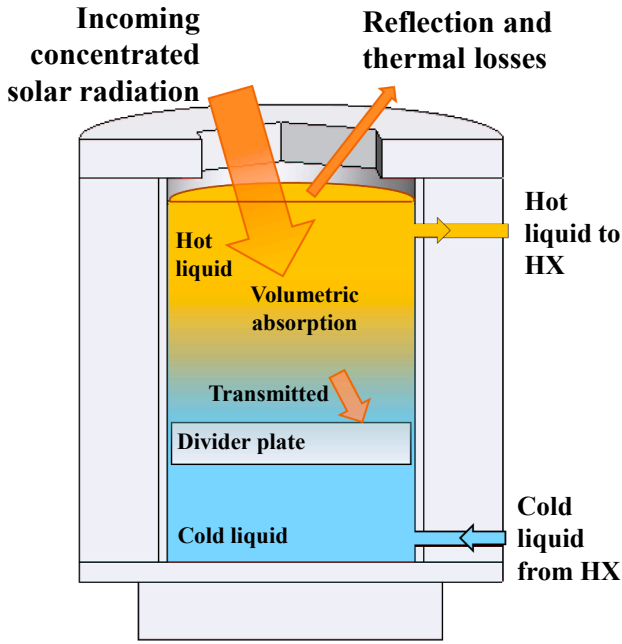


Fig. 1. Illustration of the general CSPonD concept for directly irradiated, volumetrically absorbing receiver. An open tank of molten salt is directly irradiated by concentrated solar radiation. A small fraction is reflected at the surface and the remaining fraction penetrates the open surface of the molten salt where it is absorbed volumetrically. The transmitted fraction unabsorbed by the salt is absorbed at the bottom (divider plate in the CSPonD design).

volumetrically absorbing solar receiver with integral energy storage. The design uses heliostats to concentrate and direct solar power to a large open insulated tank of molten salt. Standard methods for reducing losses in this design such as reflective cavities (Reynolds et al., 2004; Weinstein et al., 2014) and windows (Cui et al., 2013; Singh et al., 2010) cannot readily be implemented, and their effectiveness is limited due to fabrication, cost, and operation constraints especially in a desert environment (Codd, 2011; Epstein et al., 1999).

Here we introduce a new modular floating cover for open-tank, high temperature volumetric solar-thermal receivers, comprising an array of densely packed, floating hollow fused silica spheres. The advantages of transparent packed silica beads for insulating solid volumetric solar receivers have been demonstrated by Menigault et al. (1991) and Variot et al. (1994). This design uses readily available and inexpensive materials and could easily be scaled to any size. Its modular parts are easy to replace during operation, highly solar-transparent (Palik, 1997) and stable in high temperature environments. In addition, the floating parts reduce the molten salt surface area exposed to the environment, which decreases evaporation and oxidation of the fluid. This in turn decreases

damage to structural and optical components due to vapour exposure. Furthermore, as the spheres are entrained by the moving liquid surface, contaminants tends to fall off such that the spheres remain transparent. This cover concept could be applied to reduce heat losses and generate energy savings in a broad range of high temperature open bath applications including chemical and food processing, and heat-treating metals.

2. High temperature floating modular cover

Operating high temperature volumetric receivers requires significant reduction in thermal losses or high solar concentrations in order to achieve sufficiently high system efficiencies (Fletcher, 2001; Fletcher and Moen, 1977). This can be understood in terms of the receiver thermal efficiency η_{th} , defined as the ratio of collected thermal energy to total incident solar energy (Lenert and Wang, 2012), which is given by

$$\eta_{th} = \frac{\dot{Q}_{abs} - \dot{Q}_{loss}}{CG_s A_{rec}} \quad (1)$$

where \dot{Q}_{abs} is the solar power absorbed by the receiver, C is the solar concentration ratio, G_s is the direct normal irradiance, A_{rec} is the surface area of the receiver exposed to the concentrated solar irradiation, and \dot{Q}_{loss} is the sum of the convective, conductive, evaporative, and radiative heat losses to the environment. For a sufficiently deep receiver with highly absorbing containment walls, most of the non-reflected incident energy is absorbed such that $\dot{Q}_{abs} \approx (1 - R_{rec})CG_s A_{rec}$, where R_{rec} is the receiver's solar reflectance, and the thermal efficiency becomes

$$\eta_{th} \approx (1 - R_{rec}) - \frac{\dot{Q}_{conv}^{loss} + \dot{Q}_{evap}^{loss} + \dot{Q}_{rad}^{loss}}{CG_s A_{rec}} \quad (2)$$

For typical large-scale power plants with high solar concentrations, the heat loss term is small and the efficiency is dominated by the reflection losses. However, for smaller plants with lower solar concentrations, heat losses become significant with radiation dominating at high temperatures. It is therefore critical to develop methods for mitigating thermal losses without significantly increasing reflection losses.

Fig. 2 shows the heat transfer processes involved in a volumetric receiver used with CSP technology, with and without a cover. Solar salt (40 wt% KNO_3 :60 wt% $NaNO_3$ binary nitrate molten salt mixture) is semi-transparent in the visible spectrum such that it absorbs solar energy volumetrically, and has a long wavelength absorption band beginning near $2 \mu m$ and extending into the mid-infrared spectrum such that it behaves as an opaque blackbody radiator in its emission spectrum. Fused silica is nearly transparent to solar energy and allows it to be transmitted to the molten salt receiver, whereas in the near-infrared spectrum it is partially transmitting and therefore behaves as a radiation shield. For an uncovered receiver at $800^\circ C$, radiative losses from the surface reach up to $75 kW/m^2$. For a nominal solar irradiance $G_s = 1 kW/m^2 (\approx 1 \text{ sun})$ and concentration ratio $C < 100$, the thermal

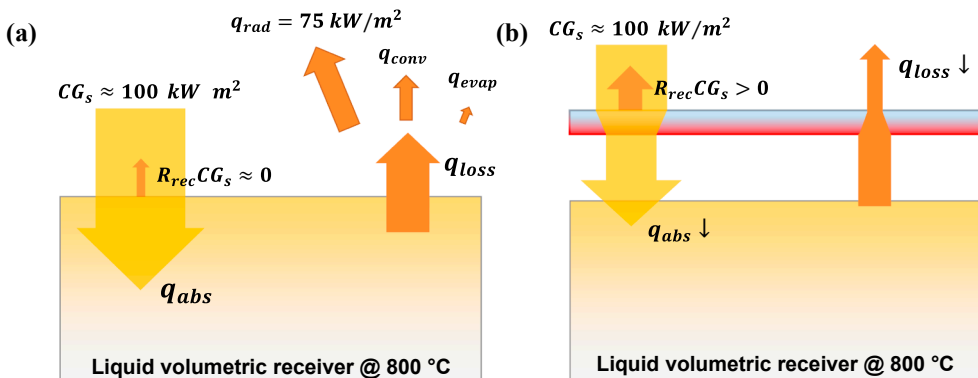


Fig. 2. Molten salt volumetric receiver energy balance without and with cover. High temperature solar-thermal volumetric receiver energy balance without (a) and with (b) solar-transparent window. For an uncovered receiver at $800^\circ C$, radiative losses from the surface reach up to $75 kW/m^2$ for an isothermal fluid contained in a vessel material with high emissivity. For a nominal solar flux $G_s = 1 kW/m^2 (\approx 1 \text{ sun})$ and concentration ratio $C < 100$, the thermal efficiency is limited to less than 25%, without accounting for transmission reflection losses.

efficiency is limited to less than 25%, without accounting for reflection losses. If a solar-transparent window was used to insulate the receiver, vapour condensation on the internal side of the window and dust on the external side would rapidly degrade the optical transmission. Furthermore, optical quality windows for relatively large receiver apertures (> 1 m-diameter) require expensive manufacturing and maintenance and are highly vulnerable to cracking.

Outdoor swimming pool owners are familiar with solar covers which have existed for decades (Czarnecki, 1963; Francey et al., 1980; Francey and Golding, 1981) and have demonstrated the ability to reduce a swimming pool’s annual heating load by 90% (Katsaprakakis, 2015). These inexpensive floating structures are similar to bubble wrap and exhibit the following key characteristics: high transparency in the solar spectrum to allow sunlight to be directly absorbed and converted to heat in the pool; high thermal resistance to minimize heat losses; and surface coverage to prevent water evaporation. Variations on the floating pool structure concept have been developed for enhanced steam generation at low solar concentrations (Ghasemi et al., 2014; Ni et al., 2016). However, their extension to high temperature fluids and volumetric solar-thermal receiver applications is accompanied by severe engineering constraints and has not been implemented to this day.

The proposed floating hollow fused silica sphere design (Fig. 3) is stable in harsh high temperature environments and is modular to allow easy online maintenance and component replacement. Similar to an outdoor pool cover, the proposed cover is highly solar-transparent, reduces convective and radiative losses, and minimizes the surface area available for evaporation losses. In addition, the self-cleaning spheres do not allow contaminants such as dust, sand particles, and condensed vapour to accumulate and remain optically clear. Unlike a single continuous window-pane, there is no limit to the surface size the spheres can cover.

3. Methodology and measurement results

The purpose of the cover is to enhance the thermal efficiency (Eq. (2)), by reducing heat losses. At high temperatures, thermal losses are dominated by radiation such that the thermal efficiency may be approximated by (Fletcher and Moen, 1977; Karni, 2012)

$$\eta_{th} \approx (1 - R_{rec}) - \frac{\dot{Q}_{rad}}{CG_s A_{rec}} \tag{3}$$

A detailed analysis of the heat loss mechanisms is included in Appendix F. For a fixed solar concentration, receiver size, and solar irradiance G_s , the quantity $CG_s A_{rec}$ remains constant, and we aim to increase efficiency by minimizing radiation thermal losses \dot{Q}_{rad} and reflection losses R_{rec} . We use experimental, analytical and numerical tools to demonstrate the floating cover concept and to determine the achievable enhancement in thermal efficiency. We first seek to predict the cover’s thermal effectiveness defined as

$$\xi_s = \frac{\text{reduction in losses}}{\text{losses for the uncovered case}} = 1 - \frac{\dot{Q}_{rad}}{\dot{Q}_{rad}^{ref}} \tag{4}$$

where \dot{Q}_{rad}^{ref} and \dot{Q}_{rad} are the thermal radiation losses to the environment from the uncovered and covered liquid, respectively. We evaluate this experimentally and use the results to validate a numerical heat transfer model. A simplified analytical thermal model capturing the effects of the various heat transfer mechanisms is developed in parallel and is used to evaluate trends in the performance in terms of the main physical and geometrical parameters. Ray-tracing simulations are carried out to evaluate the optical efficiency (solar transmission) of the cover. Finally, the receiver performance is evaluated in terms of the thermal efficiency.

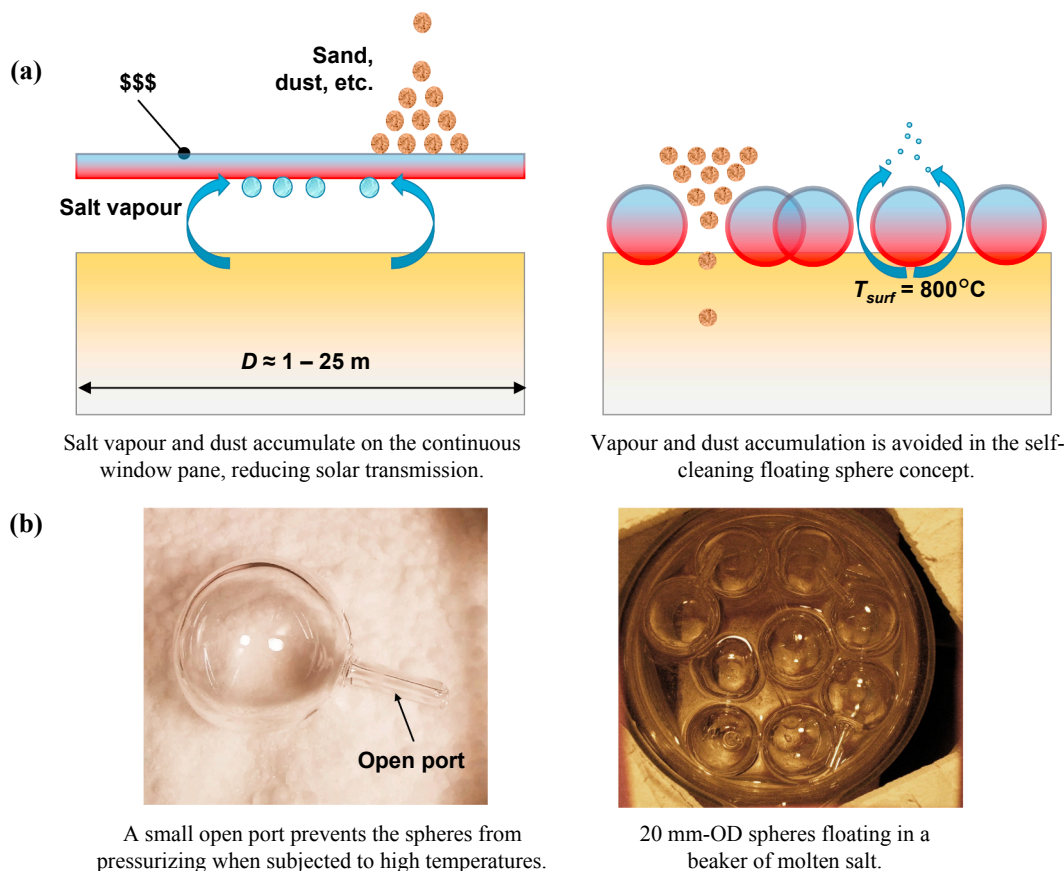


Fig. 3. Molten salt volumetric receiver cover concept. (a) Receiver operation with solar-transparent window (left) versus floating spheres (right). (b) Image of a 20 mm-OD fused silica spheres.

3.1. Laboratory experiments and simulation validation

The insulating performance of the floating spheres concept was first demonstrated experimentally in a laboratory environment. An 80 mm diameter beaker filled with a 40 wt% KNO₃:60 wt% NaNO₃ binary nitrate molten salt mixture (solar salt) was heated in a vertically oriented tube furnace such that the salt remained molten and the surface was maintained at 400 °C. Two different sizes of hollow fused silica spheres (20 mm-OD, 1.5 mm wall thickness and 70 mm-OD, 2 mm wall thickness) with open ports to prevent pressurization at high temperatures were used (Fig. 3b). The spheres were deposited one by one onto the surface of the salt immediately above the furnace such that they were heated from below by the salts only to replicate solar pond conditions. Thermal radiation losses were measured at steady-state using infrared thermography. The photon flux emanating from the surface of the salt was captured using an IRC800 Series infrared (IR) camera with a 1.0–5.3 μm spectral response range and an integration time of 0.01 s. The camera was positioned normal to the image of the surface reflected by a right-angle mirror. At 400 °C, approximately 41% of the emitted blackbody radiation falls within the camera response range. The absorption band of solar salt is expected to extend well beyond 5.3 μm and the surface of the salt therefore continues to behave as a blackbody emitter (Tetreault-Friend et al., 2017a). An image was captured with the IR camera once the surface temperature reached equilibrium. The cover's thermal effectiveness for each sphere configuration was then calculated as

$$\xi_s = 1 - \frac{\sum_{\text{all pixels}} \Phi_i}{\sum_{\text{all pixels}} \Phi_{i,\text{ref}}} \quad (5)$$

where $\Phi_{i,\text{ref}}$ and Φ_i are the photon fluxes at pixel i for the reference image without spheres and the image with spheres, respectively. Images were converted to an intensity distribution (Appendix E) as they were retrieved from the camera using an in-house calibration procedure (Bucci et al., 2016), and cropped following the edge of the molten salt beaker. Artefacts such as “dead pixels” were treated using a 2D median filter, replacing each pixel by the median intensity of the surrounding pixels enclosed in a 7-pixel wide square. A simplified diagram and images of the experimental setup are shown in Fig. 4.

Steady-state simulations were carried out using Star-CCM+, and validated vis-à-vis the experimental results. The modeled test section is shown in Fig. 4a. Combined thermal radiation and conduction heat transfer were modeled through the layer of spheres. Radiation losses are expected to dominate, therefore the surrounding air was modeled as stagnant and only radiation losses through the open top surface were accounted for such that the results are expected to be a lower limit on the performance. Solar salt is expected to be optically thick at these temperatures (Tetreault-Friend et al., 2017a) and the salt surface was therefore assumed to be opaque. “Apparent” optical properties capturing the semi-transparency of fused silica to thermal radiation were used to approximate the participating media behavior of the spherical shells in surface-to-surface radiation. Further details of the simulation methodology are included in Appendix B.

Fig. 5 presents a qualitative comparison of the experimental and simulation results for representative runs using the 20 mm spheres. The infrared images captured experimentally (Fig. 5a) correspond to the photon flux $\left(\frac{\# \text{ of photons}}{\text{m}^2 \text{ s}}\right)$ from the salt and spheres as measured by the infrared camera. The photon flux and the temperature distribution both obtained from the simulations are shown in Fig. 5b and c, respectively. The dark blue regions in each map correspond to the location of spheres, and clearly demonstrate their insulating effect such that for the same salt surface temperature, the radiation emitted at the location of the spheres is visibly reduced compared to the uncovered salt. It can be seen in both the IR images and the calculated photon flux distributions that the flux from the molten salt surface is largest at the centre where the view factor to the environment is largest and radiative cooling is the most significant, and decreases near the walls. The measured and

simulated thermal effectiveness (Eq. (4)) of the cover are compared quantitatively in Fig. 5d as a function of surface coverage φ defined as

$$\varphi = \frac{NA_{sp}^{\text{proj}}}{A_{\text{salt}}} \quad (6)$$

N is the number of spheres on the salt surface, $A_{sp}^{\text{proj}} = \pi D_s^2/4$ is the projected area of each sphere, and A_{salt} is the total surface area of the salt. Overall, there is good agreement between the experiments and simulations and the effectiveness reached a maximum of 32% for the large (70 mm) spheres. Although only one 70 mm-OD sphere could be tested experimentally in this configuration and does not correspond exactly to the expected packing fraction of the cover, the results provide insight into the insulating capabilities of the spheres and allow to validate the numerical simulations used for further analysis. Due to the confined geometry of the beaker, the 70 mm-OD sphere could achieve a higher surface coverage than the smaller 20 mm-OD spheres. The change in effective directional emissivity due to the spheres is expected to have introduced only a small source of error in the measurements given the good agreement in the results.

3.2. Large scale molten salt solar-thermal volumetric receiver performance

The validated simulation was extended to evaluate the thermal effectiveness of large-scale solar-thermal volumetric receivers. Large surfaces were approximated as infinite planes and the liquid was assumed to be densely covered with floating spheres in hexagonal closed-packed (HCP) arrangement, which provides 91% surface coverage. Ray-tracing simulations were carried out using Lambda Research TracePro 7.5.7 to evaluate the solar reflection losses R_{rec} for the covered and uncovered liquid. The infinite layer of densely packed spheres illustrated in Fig. 6 is modeled using the symmetry characteristics of the HCP arrangement. The reflection losses are calculated from the ray-tracing simulation as

$$R_{\text{rec}} = 1 - \frac{\dot{Q}_{\text{transmitted}}}{\dot{Q}_{\text{source}}} \quad (7)$$

The body of the spheres is modeled as a region with spectral refraction index n and absorption coefficient κ for fused silica as provided by Palik (Palik, 1997).

The thermal and optical analyses were carried out for sphere outer diameters from 20 to 100 mm and two different molten salt mixtures operating within different temperature ranges to characterize the effects of temperature and fluid density (sphere buoyancy). The sphere wall thicknesses were constrained to the minimum possible manufacturable thickness, as specified by the sphere manufacturer Technical Glass Products ($t = 1.5$ mm for $20 \text{ mm} \leq D_o \leq 50$ mm; $t = 2.5$ mm for $60 \text{ mm} \leq D_o \leq 100$ mm). Mixture composition, temperatures, and densities are summarized in Table 1. Further details are included in the Appendices B and D. A simple analytical model was developed to gain insight into the influence of the physical and geometrical parameters on the overall performance. The total flux through the layer q_{s-v}^{thermal} was found to be

$$q_{s-v}^{\text{thermal}} = \frac{T_s - T_v}{L} k_{\text{eff}} + \frac{\sigma(T_s^4 - T_v^4)}{\frac{1}{\epsilon_s} + \frac{1}{\epsilon_v} - 1} + \tau_v \epsilon_s \sigma(T_s^4 - T_\infty^4) \quad (8)$$

and the heat flux from the surface of the spheres to the environment $q_{v-\infty}^{\text{thermal}}$

$$q_{v-\infty}^{\text{thermal}} = h_{\text{conv}}(T_v - T_\infty) + \epsilon_v \sigma(T_v^4 - T_\infty^4) + \tau_v \epsilon_s \sigma(T_s^4 - T_\infty^4) \quad (9)$$

where T_s is the temperature of the salt surface and T_v is the temperature of a virtual surface v located immediately above the spheres with emissivity ϵ_v , reflectivity ρ_v , and transmissivity τ_v . L is the thickness of the layer of spheres above the salt, ϵ_s is the emissivity of the salt, k_{eff} is an effective thermal conductivity of the layer derived in Appendix C, and h_{conv} is the heat transfer coefficient. The analytical model gives

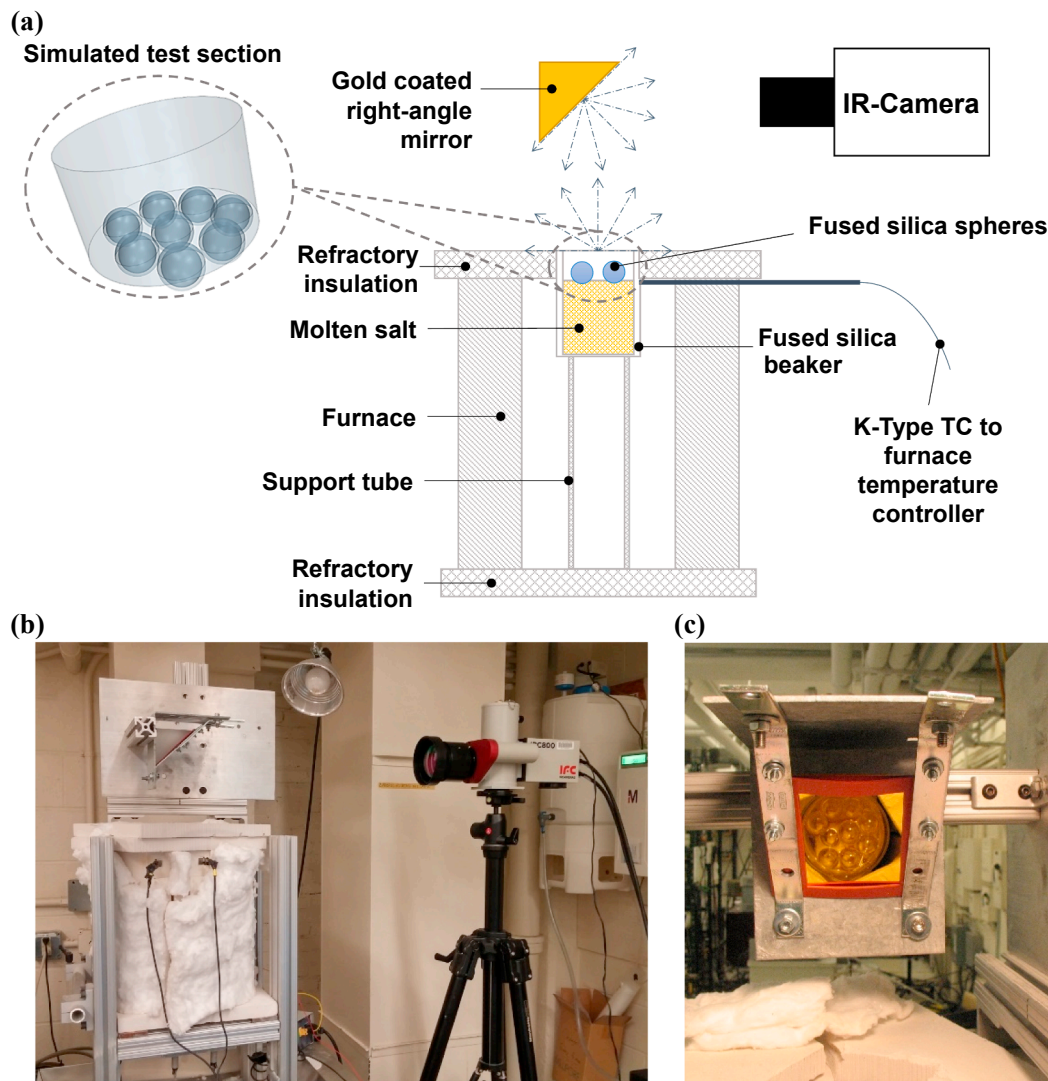


Fig. 4. Validation experiment. (a) Simplified diagram of the experimental setup used for evaluating the thermal insulation performance of the floating spheres, and 3D representation of the simulated section. An infrared camera is used to measure the photon flux losses from the surface of a heated beaker filled with molten salt, with and without floating spheres. (b and c) Image of the experimental setup (b) and of the floating spheres (c) as seen through the right-angle mirror from the infrared camera position.

insight into how the thermal losses increase with increasing sphere wall thickness, transmissivity, and emissivity, and decrease with increasing sphere diameter. Further details are provided in [Appendix C](#).

The simulation and analytical model results for the thermal effectiveness versus sphere outer diameter for the HCP cover on very large surfaces are shown in [Fig. 7a](#). The minimum effectiveness evaluated by the simulations is 21% for the smallest spheres (20 mm) at 1200 °C, and reaches a maximum of 51% for the largest spheres (100 mm) at 400 °C. The effectiveness increases with increasing conduction resistance through the spheres and increased radiation shielding. The conduction resistance increases with increasing sphere diameter, decreasing sphere wall thickness, and increasing buoyancy. The radiation shielding effectiveness increases at lower temperatures where the corresponding Planck emission spectrum of the salts shifts to longer wavelengths, and for increasing sphere wall thickness, where in both cases fused silica is more opaque to thermal radiation. Overall, the analytical model captures the same trends as the detailed simulation. The deviation is attributed to an over-predicted thermal conduction resistance. Greater agreement is expected to be achieved with more accurate treatment of the conduction geometry. Convective heat losses were neglected in this investigation and are estimated to account for approximately 25%, 12%, and 6% of the *total losses*

at 400 °C, 800 °C, and 1200 °C, respectively (see [Table F1](#)). The error introduced in the *cover's effectiveness* is less than 10% (see [Table F2](#)) over the temperature range investigated and the values reported in the present study underestimate the performance.

The optical efficiency of the cover, given as

$$\eta_{opt} = (1 - R_{rec}) \quad (10)$$

depends on the outer diameter and wall thickness of the spheres, the angular distribution of the incident irradiation, and on the buoyancy of the spheres. The dependence of the optical efficiency versus sphere outer diameter for 1.5 and 2.5 mm-thick spheres floating on nitrate and chloride molten salt mixtures is shown in [Fig. 7b](#). Two limiting uniform angular distributions are shown: half-angle $\theta = 0.27^\circ$, representative of direct solar irradiation ([Duffie and Beckman, 2013](#)), and a half-angle of $\theta = 40^\circ$, corresponding to the angular output of a representative solar concentrator. Overall, the optical efficiency is above 92% over the range studied. The cover optical efficiency initially increases with increasing diameter, followed by a gradual decay beyond 30 mm. Efficiency is highest for the incident radiation with the smallest angular distribution and on the less dense chloride salt mixture where the spheres are less buoyant. Further details are provided in [Appendix D](#).

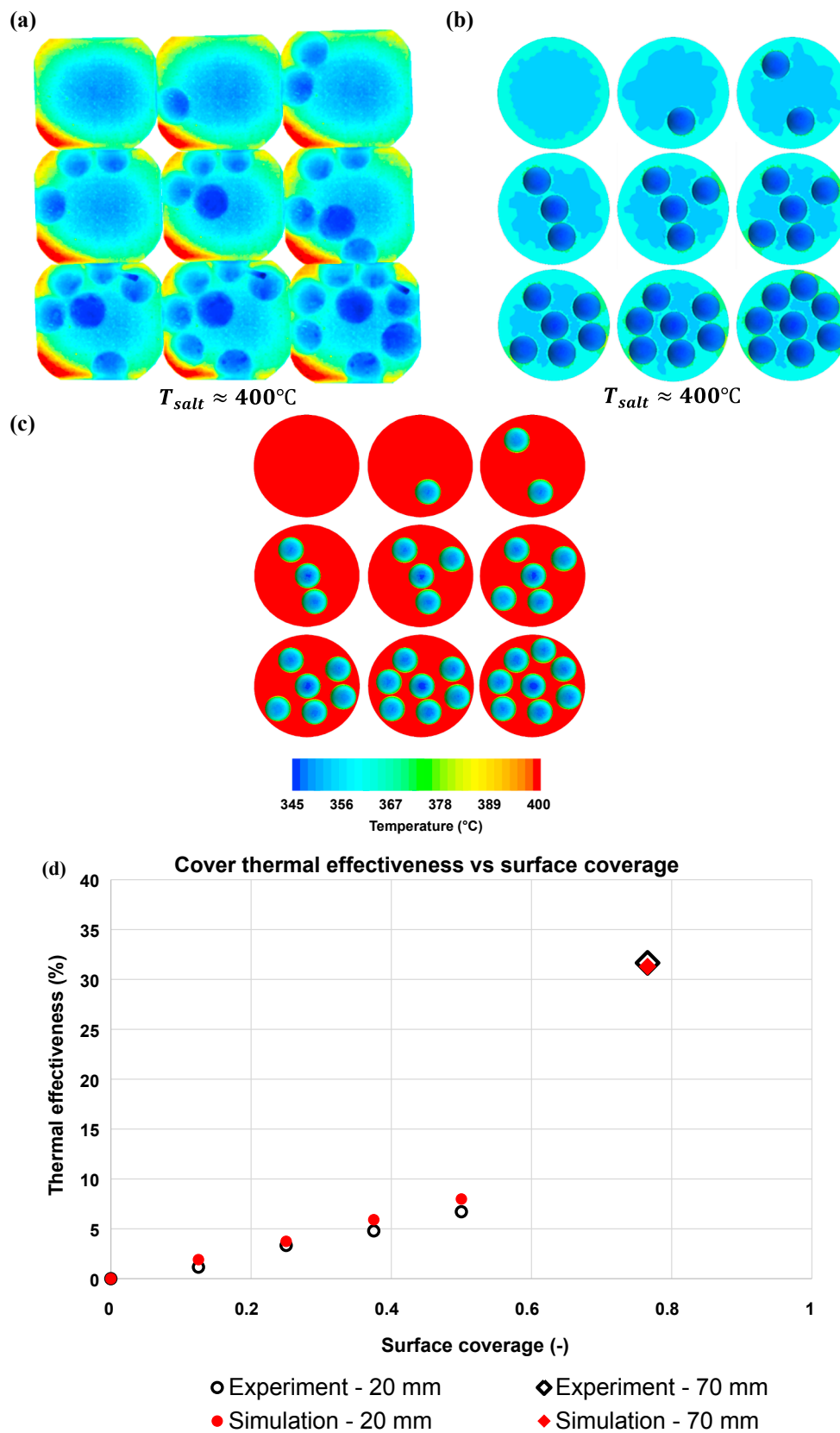


Fig. 5. Validation experiment and simulation results. (a) Photon flux map from the infrared camera. (b) Photon flux map from the simulation. (c) Temperature distribution from the simulation. (d) Calculated thermal effectiveness of floating spheres versus surface coverage in laboratory scale experiment and validation simulation. The maximum experimental error in the thermal effectiveness is 0.98 percent points for the 20 mm spheres and 4.34 percent points for the 70 mm sphere. The maximum error for the simulations is 0.45 percent points.

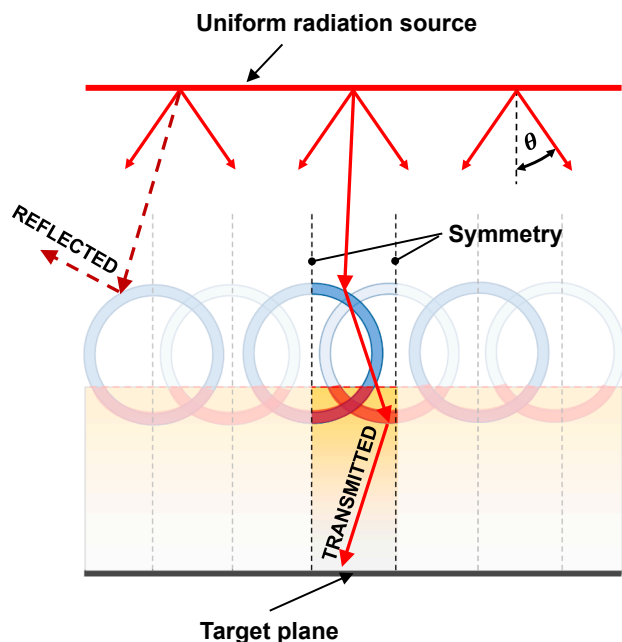


Fig. 6. Geometry, properties and boundary conditions of optical model for infinite layer of hexagonal close-packed (HCP) spheres.

3.3. Molten salt volumetric receiver thermal efficiency

The thermal efficiency versus solar concentration at temperatures within the operating ranges of binary nitrate and binary chloride molten salt mixtures, incident half-angle $\theta = 0.27^\circ$, and sphere diameters $D_o = 20$ mm and $D_o = 100$ mm are presented in Fig. 8. Natural convection is expected to reduce the reported efficiencies by less than 4% for solar concentrations above 100 (see Table F3). Evaporation losses correspond to less than 20% of a natural, unconcentrated solar irradiance $G_s \approx 1 \frac{kW}{m^2}$, and less than 1% of the total heat losses and are therefore assumed to be negligible in this analysis (Appendix F). The dashed lines correspond to thermal efficiencies without a cover. There is a clear increase in thermal efficiency for both the 20 mm and 100 mm spheres. The gains in thermal efficiency with respect to the uncovered salt increase both with increasing temperature and increasing sphere diameter. At the temperatures within the operating range of the nitrate mixture (solar salt) the cover's effectiveness is limited to larger spheres and lower solar concentrations ($C < 200$). For the higher temperature chloride mixture and larger 100 mm spheres, significant gains are predicted for solar concentrations up to $C = 1000$. In all cases, the efficiency of the uncovered salt surpasses the efficiency of the covered salt for sufficiently high solar concentrations. Under these conditions, the thermal loss term in Eq. (2) becomes negligible due to the high solar concentration C in the denominator, and the reflection losses R_{rec} introduced by the floating spheres dominates.

4. Discussion

Overall, the hollow fused silica spheres behave as excellent thermal insulators with minor reflection losses. The optimal sphere size predicted

Table 1

Molten salt mixture compositions, mean densities, temperature ranges investigated, and thermal reflectivity and solar reflectivity for the uncovered molten salt surfaces.

Molten salt mixture composition	Performance analysis temperature range	Density at mean temperature	Thermal emissivity (-)	Solar reflectivity (-)
40 wt% KNO ₃ :60 wt% NaNO ₃ binary nitrate (solar salt)	400–500 °C	1800 kg/m ³	0.89	0.11
50 wt% KCl:50 wt% NaCl binary chloride	700–1200 °C	1442 kg/m ³	0.89	0.11

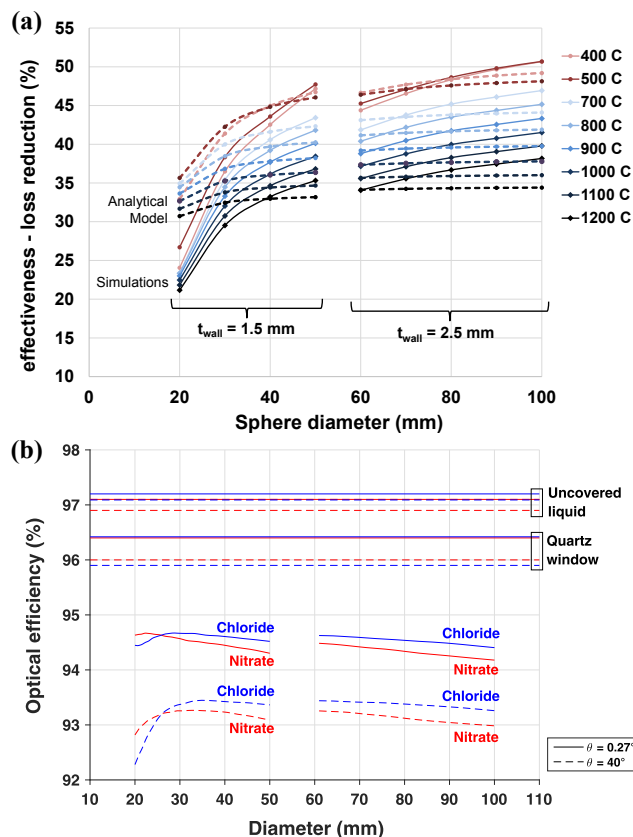


Fig. 7. Thermal and optical performance. (a) Thermal effectiveness versus sphere diameter. (b) Optical efficiency versus sphere diameter. Wall thicknesses in both (a) and (b) are 1.5 mm for diameters $D_o \leq 50$ mm, and 2.5 mm for diameters $D_o \geq 60$ mm, as specified by fused silica manufacturer.

by the analytical model is 100 mm. Increases in thermal effectiveness are negligible for larger sphere diameters, and the optical efficiency decreases slightly beyond that point. In particular, the cover increases the thermal efficiency of a receiver operating at 800 °C and 100 suns solar concentration from 23% to 54%. The larger diameter spheres demonstrate the best performance due to their combined high thermal effectiveness and optical efficiency. The thermal efficiency of molten salt receivers without a cover and with a cover of 100 mm spheres at three temperatures and four representative solar concentrations are presented in Table 2. The highest increases are observed for lower solar concentrations and low temperatures, and higher solar concentration and higher temperature. The gains in thermal efficiencies have important implications for both experimental and commercial CSP applications. The cover enables smaller facilities that do not have the solar concentration capabilities required to offset large thermal losses to operate, such as the Masdar Institute Solar Platform ($C \lesssim 100$) (Calvet et al., 2016) or the reflective tower proposed by Epstein et al. (1999) ($C \lesssim 500$). Facilities with larger solar flux concentration capabilities will still benefit from the reduction in thermal losses by reaching higher efficiencies at high temperatures, and by extending operation during hours of lower solar irradiance such as early morning, evening, and under hazy conditions. This in turn will increase

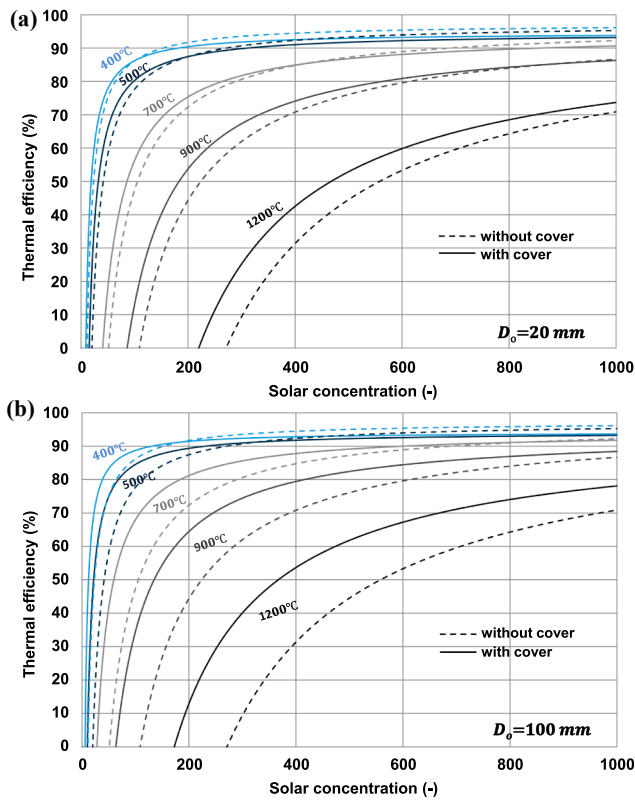


Fig. 8. Molten salt volumetric receiver thermal efficiency. Thermal efficiency with densely packed HCP cover for $D_o = 20\text{mm}$ (a), $D_o = 100\text{mm}$ spheres (b), both cases surface temperatures 400–500 °C for 40 wt% KNO_3 :60 wt% NaNO_3 binary nitrate molten salt, and 700–1200 °C for 50 wt% KCl :50 wt% NaCl binary chloride molten salt. Dashed lines represent thermal efficiencies without a cover. Incident irradiation half-angle $\theta = 0.27^\circ$.

Table 2

Comparison of thermal efficiency with no cover and with 100 mm-spheres at three operating temperatures and $C = 50, 150, 500,$ and 1000 solar concentration ratios assuming direct solar irradiance of 1 kW/m^2 . Values less than zero indicate solar concentration is less than breakeven concentration required for receiver operation.

Receiver temperature (°C)	C = 50		C = 150		C = 500		C = 1000	
	No cover	100 mm spheres						
400	75%	83%	90%	91%	95%	93%	96%	94%
800	< 0%	13%	48%	67%	82%	86%	90%	90%
1200	< 0%	< 0%	< 0%	< 0%	45%	62%	71%	78%

the down-stream efficiency of the heat engine.

The maximum possible number of spheres N required to completely cover a molten salt receiver or bath of diameter D_{salt} with HCP arranged spheres (91% surface coverage) of diameter D_o is given as

$$N \approx 0.91 \left(\frac{D_{salt}}{D_o} \right)^2 \tag{11}$$

Thus, for a 1 m-diameter solar receiver and 100 mm-diameter spheres, only 91 spheres are required to achieve maximum salt surface coverage. The total cost to cover this area using custom-made spheres at approximately US\$100/sphere is therefore US\$9100. The cost of replacing a single broken part would be only US\$100 and would not require operation downtime. In comparison, we estimate that a single continuous fused silica window would cost up to US\$250,000 and potentially the same amount to replace when broken, in addition to operation downtime. Furthermore, using prices for custom-made spheres is a conservative estimate and large scale manufacturing methods are expected to decrease costs by

approximately half, such that a floating cover would cost about US\$4550. Large-scale low cost production of the floating spheres could be attained using automated light-bulb manufacturing techniques, where a standard ribbon machine (Cable, 1999) could be altered to operate at higher temperature for fused silica fabrication. Other shapes such as cylinders with pinched ends could be considered to further reduce costs, increase optical efficiency, and increase surface coverage, which in turn will further improve insulation. Surface coverage could also be increased to approach 100% using smaller spheres to fill the interstitial voids. In addition, methods for sealing the open ports at high temperatures to avoid contamination inside the spheres, material thermal stability and compatibility, and transparency reduction over time should all be investigated. Although contaminant suspensions such as sand may fall through the cover’s void spaces and contribute to the volumetric absorption of the salt, they are expected to settle to the bottom over time (Tetreault-Friend et al., 2017b). Other heat loss mechanisms should be investigated further; in particular evaporation losses, which can potentially be reduced by 90% with densely packed spheres and will reduce the cost of adding makeup salt. The floating fused silica spheres can also be beneficial in broad salt bath applications. The modular components facilitate maintenance and allow varying the surface coverage of the insulation to accommodate a variety of application sizes, and the transparent insulation allows seeing inside the bath during manufacturing processes. In addition, fused silica has a higher conduction resistance than materials such as stainless steels and ceramics and is therefore a better insulator.

5. Conclusions

We have demonstrated a simple, efficient, and robust floating structure that can be scaled to any size and used to insulate and significantly increase the thermal efficiency of high temperature molten salt volumetric receivers. The floating cover consists of hollow fused silica spheres that reduce thermal losses up to 51% while reducing the optical efficiency by less than 5%. This cover structure can enable the use of high temperature molten salt volumetric receivers in new operating regimes such as lower solar concentrations, higher efficiency at higher temperatures, and ex-

tending operation during hours of low solar irradiance. The cover structure concept could also be applied to a wide range of high temperature open bath applications to generate energy savings. Examples include molten salt bath furnaces for heat treating metals and curing plastics and rubbers, fryers for food processing, and oil baths for chemical processing applications.

Acknowledgements

The authors dedicate this work to the late Dr. Thomas McKrell, a gentle force who will be remembered as a great scientist, mentor, and friend.

This work was supported by the Cooperative Agreement between the Masdar Institute of Science and Technology (Masdar Institute), Abu Dhabi, UAE and the Massachusetts Institute of Technology (MIT), Cambridge, MA, USA - Reference 02/MI/MIT/CP/11/07633/GEN/G/00.

Appendix A. Nomenclature

Symbol	Description	Typical units
A_{rec}	Surface area of the receiver exposed to solar irradiance	m^2
C	Solar concentration ratio	–
D_o	Sphere outer diameter	mm
F	View factor	–
g	Gravitational acceleration	$m\ s^{-2}$
G_s	Solar irradiance	$kW\ m^{-2}$
h_{conv}	Convective heat transfer coefficient	$W\ m^{-2}\ K^{-1}$
\bar{h}_{nc}	Heat transfer coefficient for natural convection	$W\ m^{-2}\ K^{-1}$
H_{sink}	Sink depth	mm
H_{cyl}	Cylinder length	mm
ΔH^{vap}	Enthalpy of vaporization	Jg^{-1}
$I_{b\lambda}$	Spectral blackbody intensity	$W\ m^{-2}\ \mu m^{-1}$
k	Thermal conductivity	$W\ m^{-1}\ K^{-1}$
L	Thickness of equivalent insulation layer	mm
l	Characteristic length of receiver for convection	m
\dot{m}	Rate of mass transfer	$kg\ s^{-1}$
n	Refractive index	–
N	Number of spheres	–
\bar{Nu}_l	Average Nusselt number	–
Pr	Prandtl number	–
q	Heat flux	$kW\ m^{-2}$
\dot{Q}	Rate of heat transfer	kW
R	Thermal resistance	$K\ W^{-1}$
R_{rec}	Receiver solar reflectance	–
Ra_l	Rayleigh number	–
\bar{s}	Average path length	mm
t	Wall thickness	mm
T	Temperature	$^{\circ}C$
\bar{T}_{op}	Average operating temperature	$^{\circ}C$
<i>Greek letters</i>		
β	Coefficient of thermal expansion	K^{-1}
ϵ	Emissivity	–
κ	Extinction index	–
λ	Wavelength	μm
ν	Kinematic viscosity	$m^2\ s^{-1}$
η_c	Capture efficiency	–
η_{th}	Thermal efficiency	–
θ	Irradiation half-angle	$^{\circ}$
ξ_s	Cover thermal effectiveness	–
ρ	Reflectivity	–
ρ^*	Apparent reflectivity	–
$\rho_{ }$	Parallel-polarized reflectivity component	–
ρ_{\perp}	Perpendicular-polarized reflectivity component	–
σ	Stefan-Boltzmann constant	$W\ m^{-2}\ K^{-4}$
τ_{rec}	Receiver transmittance	–
τ	Transmissivity	–
τ^*	Apparent transmissivity	–
φ	Surface coverage	–
Φ_i	Photon flux at pixel i	$m^{-2}\ s^{-1}$
<i>Subscripts</i>		
abs	Absorption	
$cond$	Conduction heat transfer	
$conv$	Convective heat transfer	
eff	Effective	
$evap$	Evaporative losses	
cyl	Cylinder	
i	Pixel index	
$loss$	Thermal loss	
$proj$	Projected surface	

<i>rad</i>	Radiative heat transfer
<i>rec</i>	Receiver air-salt interface
<i>ref</i>	Reference situation with no cover
<i>s</i>	Molten salt surface
<i>salt</i>	Salt surface
<i>salt – sphere</i>	Salt-sphere interface
<i>sp</i>	Sphere
<i>tot</i>	Total
<i>v</i>	Virtual surface
∞	Environment
Abbreviations	
IR	Infrared
OD	Outside diameter
VHT	Very high temperature

Appendix B. Computational thermal model

Steady-state simulations were developed and carried-out in Star-CCM+ and were validated with the experimental results. Combined heat transfer including both thermal radiation and conduction were included inside the system. The surrounding air is modeled as a solid such that the results are expected to be a lower limit on the performance. The geometry and boundary conditions are shown in Fig. B.1. Only radiation thermal losses through the open top surface are accounted for. Both sphere sizes used in the experiments were modeled. For the smaller, 20 mm-OD spheres, three different configurations were randomly generated to determine the effects of uncertainty in sphere position and the results were averaged. The standard deviation in the simulations results from the three randomly generated configurations was 44% for the case of the salt cover with a single 20 mm-OD sphere, and less than 10% for all other cases. The approximate depth to which the spheres sink, H_{sink} , was calculated from a simple buoyancy balance as an initial estimate. The effectiveness of the spheres was then calculated as

$$\xi_s = 1 - \frac{\dot{Q}_{loss}^{rad}}{\dot{Q}_{loss,ref}^{rad}} \tag{B.1}$$

where \dot{Q}_{loss}^{rad} and $\dot{Q}_{loss,ref}^{rad}$ are the radiation thermal losses escaping the system through the open top surface for the covered liquid and reference uncovered liquid systems, respectively.

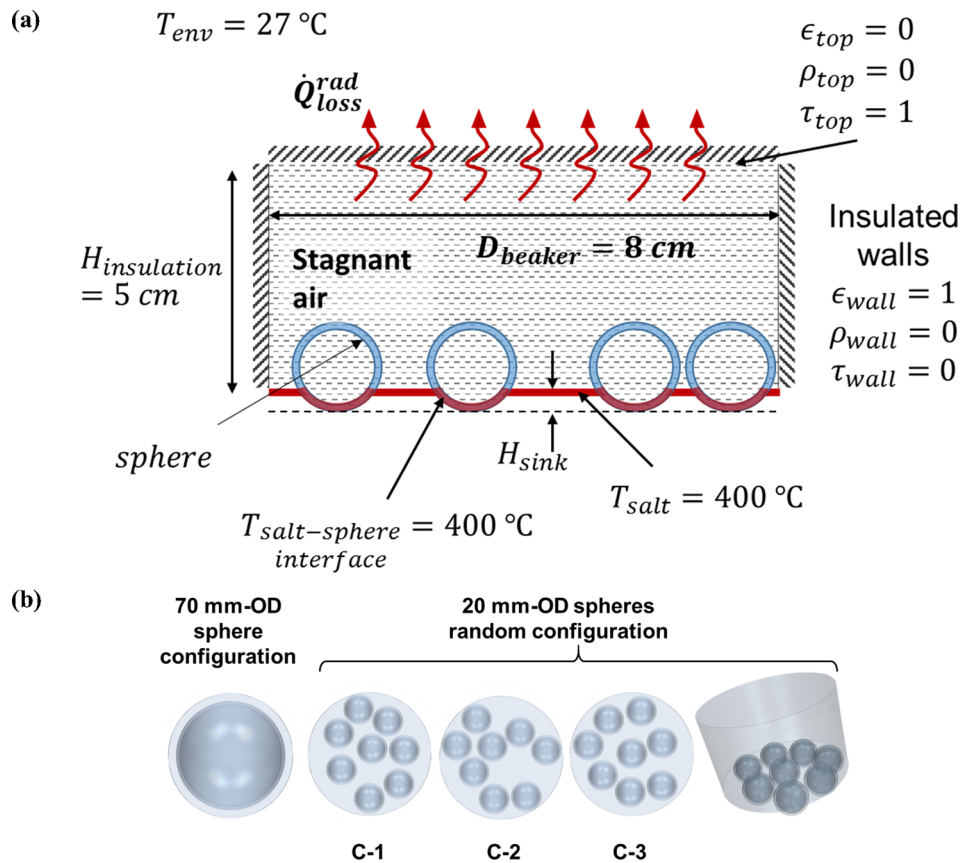


Fig. B1. (a) Cross-sectional representation of the modeled region with properties, and boundary conditions of thermal model. (b) Modeled section in the simulation showing three distinct sphere configurations. The results for the three configurations are averaged for comparison and validation with the experimental results.

The salt is modeled as an opaque medium with spectrally averaged emissivity $\epsilon_{salt} = 0.89$ (Tetreault-Friend et al., 2017a). Solar salt is expected to be optically thick at these temperatures (Tetreault-Friend et al., 2017a) and the surface can be approximated as a black-body emitter. Fused silica has a long-wavelength absorption band which begins around 2.5 μm . As temperature increases, the Planck emission spectrum peak moves from longer to shorter wavelengths, moving out of the absorption band and into the semi-transparent region. Fused silica therefore behaves as a participating media and its average optical properties vary with temperature. Nevertheless, the thermal radiation is treated as diffuse, gray, surface-to-surface radiation throughout the system. “Apparent” optical properties capturing the radiation properties of semi-transparent fused silica were evaluated to model the spherical shells with finite wall thickness as a single surface for the radiative heat transfer component. The spectral emissivity ϵ_λ , apparent reflectivity ρ_λ^* , and apparent transmissivity τ_λ^* of the single surface are given by McMahon (1950):

$$\epsilon_\lambda = \frac{[1 - \rho_\lambda][1 - \tau_\lambda]}{1 - \rho_\lambda \tau_\lambda} \tag{B.2}$$

$$\rho_\lambda^* = \rho_\lambda \left\{ 1 + \frac{\tau_\lambda^2 [1 - \rho_\lambda]^2}{1 - \rho_\lambda^2 \tau_\lambda^2} \right\} \tag{B.3}$$

$$\tau_\lambda^* = \tau_\lambda \frac{[1 - \rho_\lambda]^2}{1 - \rho_\lambda^2 \tau_\lambda^2} \tag{B.4}$$

which together satisfy Kirchhoff’s law $\epsilon_\lambda + \rho_\lambda^* + \tau_\lambda^* = 1$. The spectral hemispherically averaged true transmissivity τ_λ is obtained by evaluating the following expression

$$\tau_\lambda = e^{-\frac{4\pi n \bar{s}}{\lambda}} \tag{B.5}$$

where \bar{s} is the average path length through the thickness of the fused silica walls. For this study, we take this to be the minimum possible path length, $\bar{s} = t$ (wall thickness), which yields the highest possible transmission for thermal radiation and provides a lower limit on the performance.

The spectral, hemispherical, true reflectivity ρ_λ is given by Dunkle (1963)

$$\rho_\parallel = 1 - \frac{8n}{n^2 + \kappa^2} \left\{ 1 - \frac{n}{n^2 + \kappa^2} \ln[(n + 1)^2 + \kappa^2] + \frac{n^2 - \kappa^2}{\kappa(n^2 + \kappa^2)} \tan^{-1} \frac{\kappa}{n + 1} \right\} \tag{B.6}$$

$$\rho_\perp = 1 - 8n \left[1 - n \ln \frac{(n + 1)^2 + \kappa^2}{n^2 + \kappa^2} + \frac{n^2 - \kappa^2}{\kappa} \tan^{-1} \frac{\kappa}{n(n + 1) + \kappa^2} \right] \tag{B.7}$$

$$\rho_\lambda = \frac{1}{2}(\rho_\parallel + \rho_\perp) \tag{B.8}$$

where $n = n(\lambda)$ is the refractive index and $\kappa = \kappa(\lambda)$ is the extinction index. We assume smooth and flat surfaces due to large sphere radii (Boriskina et al., 2016). For gray thermal radiation, emission-spectrum weighted averaged quantities are evaluated as

$$\epsilon_{sp}(\bar{T}_{op} = 400^\circ\text{C}) = \frac{\int_0^\infty I_{b\lambda}(\bar{T}_{op}) \epsilon_\lambda d\lambda}{\int_0^\infty I_{b\lambda}(\bar{T}_{op}) d\lambda} \tag{B.9}$$

$$\rho_{sp}(\bar{T}_{op} = 400^\circ\text{C}) = \frac{\int_0^\infty I_{b\lambda}(\bar{T}_{op}) \rho_\lambda^* d\lambda}{\int_0^\infty I_{b\lambda}(\bar{T}_{op}) d\lambda} \tag{B.10}$$

$$\tau_{sp}(\bar{T}_{op} = 400^\circ\text{C}) = \frac{\int_0^\infty I_{b\lambda}(\bar{T}_{op}) \tau_\lambda^* d\lambda}{\int_0^\infty I_{b\lambda}(\bar{T}_{op}) d\lambda} \tag{B.11}$$

where $I_{b\lambda}(\bar{T}_{op})$ is the spectral blackbody intensity at the operating temperature $\bar{T}_{op} = 400^\circ\text{C}$. Using spectral values for n and κ from Palik (1997), the calculated properties for the experimental validation simulations are reported in Table B1.

The validated thermal model is then extended to evaluate the performance of the modular cover on very large surfaces. Large surfaces are approximated as infinite in the plane of the liquid’s surface with hexagonal close-packed spheres (91% surface coverage). To reduce computational time, a single lattice is modeled with symmetric boundaries as shown in Fig. B.2. The simulations were carried out for sphere outer diameters 20–100 mm. The sphere wall thickness was constrained to the minimum possible manufacturable thickness, as specified by the fused silica sphere manufacturer’s specifications.

Table B1
Geometrical parameters and calculated properties for experimental validation simulations.

D_o (mm)	20	70
t (mm)	1.5	2.0
H_{sink} (mm)	11	22
ρ_{sphere}	0.7651	0.7740
τ_{sphere}	0.1628	0.1621
τ_{sphere}	0.0721	0.0640
salt–sphere	0.8432	0.8432
$\rho_{\text{salt–sphere}}$	0.1568	0.1568
$\tau_{\text{salt–sphere}}$	0	0

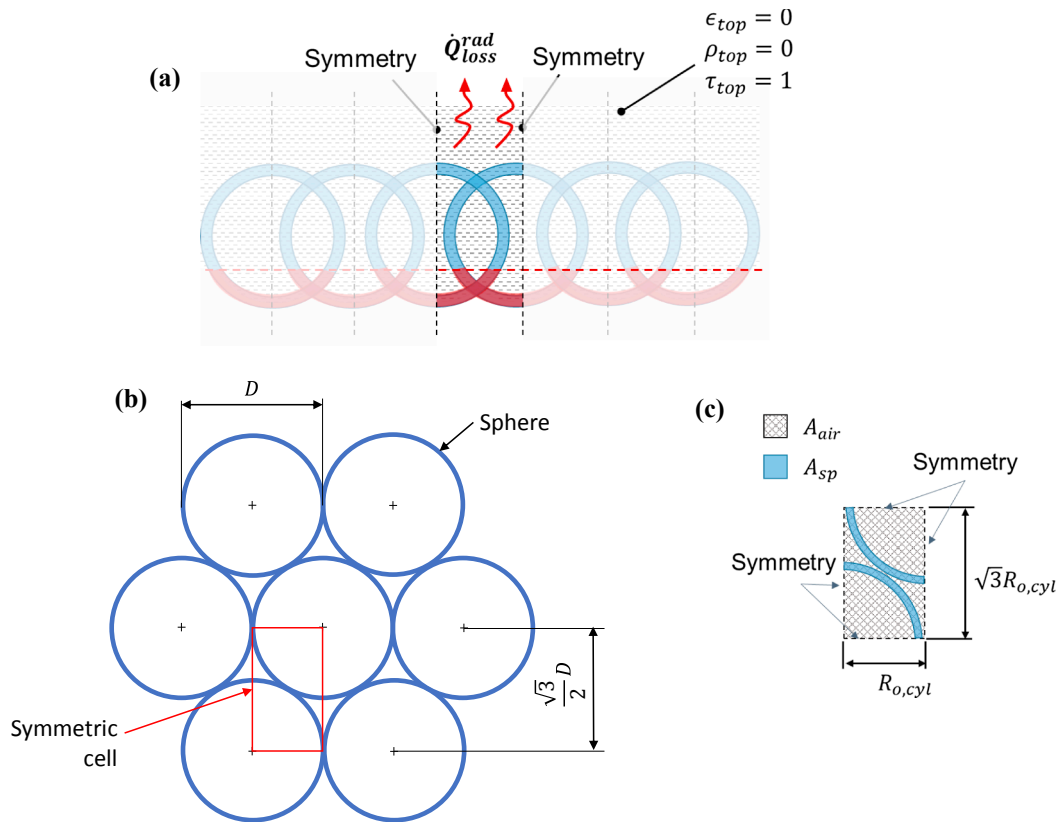


Fig. B2. Geometry, properties, and boundary conditions of thermal model for infinite layer of hexagonal close-packed (HCP) spheres.

Appendix C. Analytical thermal model

A simplified analytical thermal model capturing the effects of the various heat transfer mechanisms in a cover of an infinite layer of hexagonal close-packed (HCP) spheres, as shown in Fig. B2, can be used to understand and discuss the performance of the cover in terms of the physical and geometrical parameters.

We define a virtual surface v located immediately above the layer of spheres as shown in Fig. C1. The total heat flux $q_{loss}^{thermal}$ leaving the salt surface flows through two layers before reaching the ambient environment: from the salt surface to the virtual surface $q_{s-v}^{thermal}$, and from the virtual surface to the ambient $q_{v-\infty}^{thermal}$.

$$q_{loss}^{thermal} = q_{s-v}^{thermal} = q_{v-\infty}^{thermal} \tag{C.1}$$

The heat flux through the layer of spheres may be decomposed into radiative and conduction components in a decoupled parallel approach as illustrated in the equivalent circuit in Fig. C1, such that

$$q_{s-v}^{thermal} = q_{s-v}^{cond} + q_{s-v}^{rad} + q_{s-\infty}^{rad,tr} \tag{C.2}$$

where q_{s-v}^{cond} and q_{s-v}^{rad} are the conduction and radiation heat flux components through the sphere layer, respectively, and $q_{s-\infty}^{rad,tr}$ is the radiative heat flux transmitted directly through the layer to the ambient. Similarly, the heat flux from the virtual surface to the ambient is decomposed into radiative and convective component as

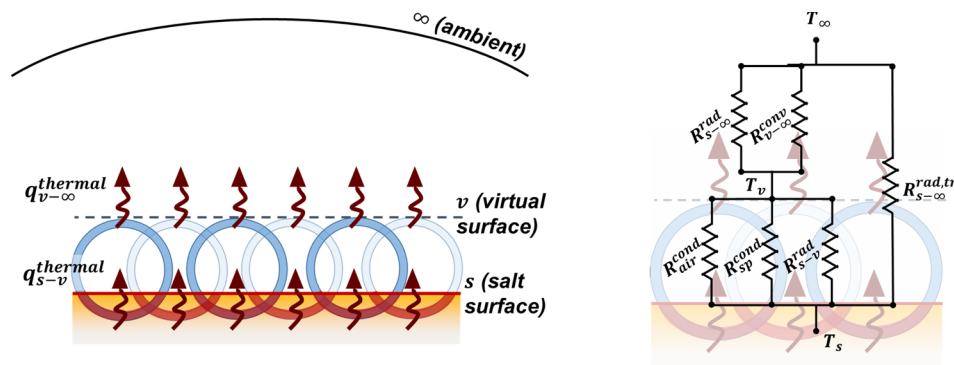


Fig. C1. Diagram illustrating the simplified analytical model.

$$q_{v-\infty}^{thermal} = q_{v-\infty}^{conv} + q_{v-\infty}^{rad} + q_{s-\infty}^{rad,tr} \tag{C.3}$$

where again $q_{v-\infty}^{conv}$ and $q_{v-\infty}^{rad}$ are the conduction and radiation heat flux components through the sphere layer, respectively, and $q_{s-\infty}^{rad,tr}$ is the radiative heat flux transmitted directly through the layer to the ambient. We begin our analysis with the heat flow through the layer of spheres. The conduction and radiation transport are coupled by the temperature gradient through the layer. For a densely packed array of spheres, the view factor from the salt to the infinite layer of spheres will approach unity. We therefore approximate the layer as a single infinite parallel plane above the salt surface at the location of the virtual surface. The plane is taken to be a semi-transparent window with emissivity ϵ_v , reflectivity ρ_v , and transmissivity τ_v , and view factor $F_{s-v} \approx 1$. The radiative heat flux can simply be expressed

$$q_{s-v}^{rad} = \frac{\sigma(T_s^4 - T_v^4)}{\frac{1-\epsilon_s}{\epsilon_s} + \frac{1}{F_{s-v}} + \frac{1-\epsilon_v}{\epsilon_v}} = \frac{\sigma(T_s^4 - T_v^4)}{\frac{1}{\epsilon_s} + \frac{1}{\epsilon_v} - 1} \tag{C.4}$$

where T_s is the temperature of the salt surface and T_v is the temperature of the virtual surface. The transmitted component through the layer assuming radiation contribution from the environment is negligible, is simply given as

$$q_{s-\infty}^{rad,tr} = \tau_v \epsilon_s \sigma T_s^4 \tag{C.5}$$

We now consider the conduction heat transfer component through the layer

$$\dot{Q}_{s-v}^{cond} = \frac{T_s - T_v}{R_{s-v}^{cond}} \tag{C.6}$$

where R_{s-v}^{cond} is the thermal conduction resistance of the layer. As a first approximation, we simplify the geometry from spheres to open top and bottom cylinders as shown in Fig. C2.

In the simplified system, we assume $D_{o,cyl} = D_{o,sp}$, $H_{cyl} = D_{o,sp}$, $t_{cyl} = t_{sp}$, and $H_{sink,cyl} = H_{sink,sp}$. The thermal conduction resistance may readily be evaluated for the new configuration by analyzing a parallel circuit through the air layer and cylinder walls

$$\frac{1}{R_{s-v}^{cond}} = \frac{1}{R_{air}^{cond}} + \frac{1}{R_{cyl}^{cond}} \tag{C.7}$$

$$R_{air}^{cond} = \frac{L}{k_{air} A_{air}} R_{cyl}^{cond} = \frac{L}{k_{sp} A_{cyl}^{proj}} \tag{C.8}$$

We take the thickness of the insulation layer between the salt and virtual surface to be $L = H_{cyl} - H_{sink,cyl}$. We find the heat flux from conduction to be

$$q_{s-v}^{cond} = \frac{\dot{Q}_{s-v}^{cond}}{A_{tot}} = \frac{T_s - T_v}{A_{tot}} \left(\frac{1}{R_{air}^{cond}} + \frac{1}{R_{cyl}^{cond}} \right) = \frac{T_s - T_v}{L} \left(\frac{k_{air} A_{air}}{A_{tot}} + \frac{k_{cyl} A_{cyl}^{proj}}{A_{tot}} \right) = \frac{T_s - T_v}{L} [(1 - \phi_{cyl})k_{air} + \phi_{cyl}k_{cyl}] = \frac{T_s - T_v}{L} k_{eff} \tag{C.9}$$

where k_{air} and k_{cyl} are the thermal conductivities of air and the cylinder (sphere) material (fused silica), respectively, k_{eff} is the effective thermal conductivity of the layer, A_{tot} is the total surface area of the symmetric cell projected onto the plane of the virtual surface, expressed as the sum of the projected areas of the air and cylinders such that $A_{tot} = A_{air} + A_{cyl}^{proj}$, and $\phi_{cyl} = \frac{A_{cyl}^{proj}}{A_{tot}}$.

We evaluate ϕ_{cyl} taking the symmetric cell shown in Fig. B2 with two quarter cylinders:

$$\phi_{cyl} = \frac{A_{cyl}^{proj}}{A_{tot}} = \frac{2 \times \frac{1}{4} \pi (R_{o,cyl}^2 - R_{i,cyl}^2)}{R_{o,cyl} \times \sqrt{3} R_{o,cyl}} = \frac{\pi}{2\sqrt{3}} \left(1 - \frac{R_{i,cyl}^2}{R_{o,cyl}^2} \right) = \frac{\pi}{2\sqrt{3}} \left[1 - \left(1 - \frac{t_{cyl}}{R_{o,cyl}} \right)^2 \right] \tag{C.10}$$

The effective thermal conductivity of the layer is thus given by

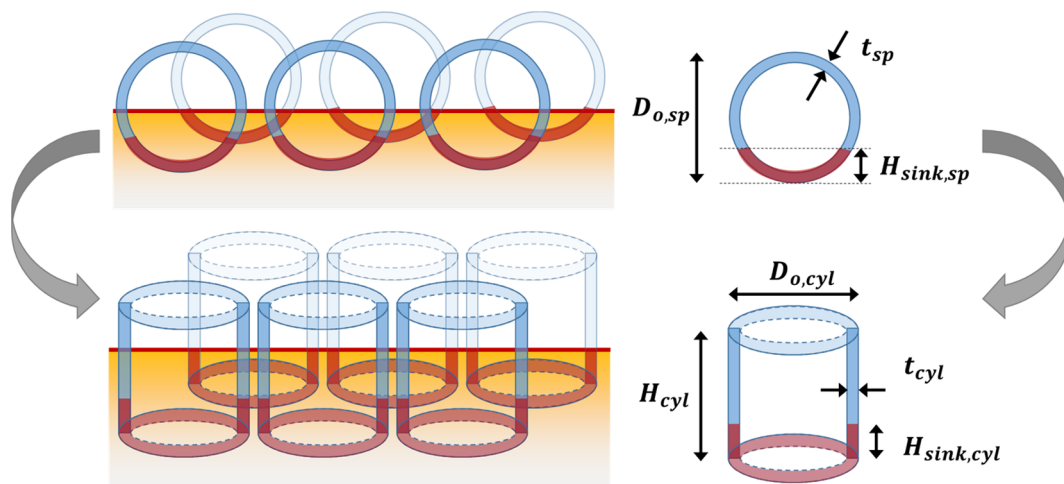


Fig. C2. Simplified geometry for conduction through layer of spheres.

$$k_{eff} = (1 - \phi_{cyl})k_{air} + \phi_{cyl}k_{cyl} = \frac{\pi(k_{cyl} - k_{air})}{2\sqrt{3}} \left[1 - \left(1 - \frac{t_{cyl}}{R_{o,cyl}} \right)^2 \right] + k_{air} \tag{C.11}$$

Eqs. (C.10) and (C.11) may be substituted into Eq. (C.9) to solve for the conductive heat flux through the layer of spheres q_{s-v}^{cond} . Finally, the total flux through the layer is given as

$$q_{s-v}^{thermal} = \frac{T_s - T_v}{L} k_{eff} + \frac{\sigma(T_s^4 - T_v^4)}{\frac{1}{\epsilon_s} + \frac{1}{\epsilon_v} - 1} + \tau_v \epsilon_s \sigma T_s^4 \tag{C.12}$$

We now consider the second layer, from the virtual surface to the ambient environment. We take the ambient to be a perfect absorber and the view factor from the virtual surface to the ambient environment to be $F_{v-\infty} = 1$. The thermal radiation emitted to the environment is therefore expressed as

$$q_{v-\infty}^{rad} = \epsilon_v \sigma (T_v^4 - T_\infty^4) \tag{C.13}$$

where T_∞ is the temperature of the surrounding ambient environment. The transmitted thermal radiation is identical to the transmitted component through the layer of spheres and is given in Eq. (C.5). Finally, the convective heat flux is expressed as

$$q_{v-\infty}^{conv} = h_{conv} (T_v - T_\infty) \tag{C.14}$$

where h_{conv} is the convective heat transfer coefficient. In this study, we assume thermal radiation to dominate the thermal losses to the environment as in the computational model and let $h_{conv} \approx 0$. For a more rigorous analysis, we may obtain the heat transfer coefficient from standard Nusselt number correlations for heated horizontal plates facing upwards. Finally, the total heat flux from the virtual surface to the environment is given by

$$q_{v-\infty}^{thermal} = h_{conv} (T_v - T_\infty) + \epsilon_v \sigma (T_v^4 - T_\infty^4) + \tau_v \epsilon_s \sigma T_s^4 \tag{C.15}$$

Eqs. (C.12) and (C.15) may be substituted into Eq. (C.1) and solved numerically for the thermal losses $q_{loss}^{thermal}$ from the salt and the intermediate virtual surface temperature T_v .

Appendix D. Optical efficiency modeling

Ray-tracing simulations in Lambda Research TracePro 7.5.7 are used to estimate the optical efficiency of concentrated solar radiation across an

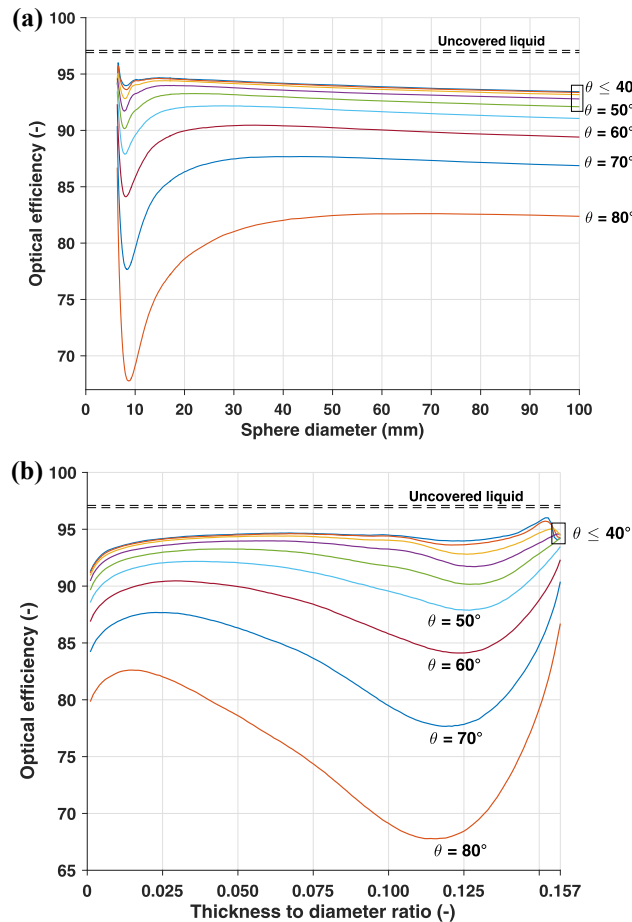


Fig. D1. Optical efficiency on binary nitrate molten salt. (a) Based on a sphere wall thickness of 1 mm. (b) as a function of the ratio of the sphere wall thickness-to-diameter ratio. The optical efficiency of the uncovered liquid is indicated for a solar angular distribution (97.1%), and $\theta = 40^\circ$ (96.9%).

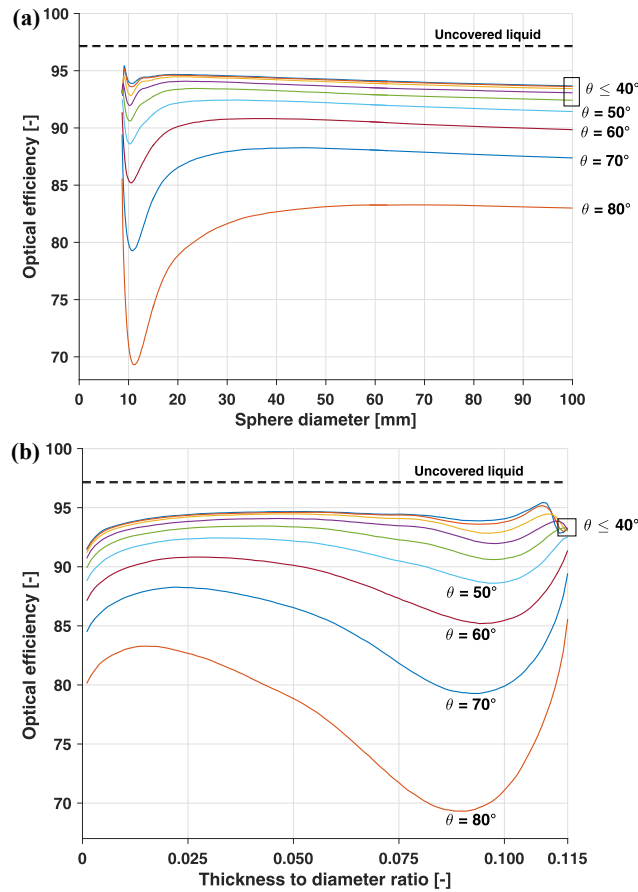


Fig. D2. Optical efficiency on binary chloride molten salt. (a) Based on a sphere wall thickness of 1 mm. (b) More generally, as a function of the ratio of the sphere wall thickness to its diameter. The optical efficiency of the uncovered liquid is indicated for a solar angular distribution (97.2%), and $\theta = 40^\circ$ (97.1%).

infinite sphere array as illustrated in Fig. 6. According to their buoyancy on molten salts, the spheres are partially immersed in a volume with the refractive index of either nitrate ($n = 1.41$) or chloride ($n = 1.40$) molten salts (Tetreault-Friend et al., 2017a). The depth to which the spheres sink depends on the diameter and wall thickness of the spheres and the respective densities of the molten salt mixtures (Table 1), which in turn produces slightly different efficiencies for each mixture. Rays are generated from a plane above the sphere array and follow the solar spectral wavelength distribution (ASTM E490-00a(2014), Standard Solar Constant and Zero Air Mass Solar Spectral Irradiance Tables). The intensity is constant and uniform over the entire plane source and at all angles within the cone defined by the specified half-angle θ (c.f., Fig. 6). The power refracted into the molten salts is measured as the power incident on the lower face of the molten salts volume. The inputs to each simulation are the irradiation half-angle (θ), the diameter of the spheres (D), and their thickness (t). Using 10^6 rays in each simulation, the relative standard deviation on the optical efficiency is measured below 0.3% on the simulation results. The geometry of the system allows to report the cover optical efficiency as a function only of the t/D ratio and θ . Figs. D1 and D2. show the optical efficiency through modular fused silica covers which rest on either nitrate or chloride molten salts.

In all cases, optical efficiency decreases as the angular spread of the irradiation increases. For each irradiation angular distribution, optical efficiency has two local maxima. As the spread of the irradiation increases, the first local maximum is found at increasingly lower t/D values, whereas the second local maximum is found at larger t/D values. Additionally, the distance between the maxima increases and the second maximum becomes dominant. For nitrate molten salts, the absolute optical efficiency maximum for each irradiation angular distribution occurs always at high t/D values, near the sinking point of the spheres. For chloride molten salts, the largest optical efficiency is exceptionally found at low t/D values for a small range of irradiation half-angles, and otherwise at high t/D values.

Appendix E. Conversion of photon counts to heat flux ratio

The effectiveness of the cover was previously given in Eq. (5) as

$$\xi_s = 1 - \frac{\sum_{\text{all pixels}} \Phi_i}{\sum_{\text{all pixels}} \Phi_{i,ref}} \tag{5}$$

where Φ_i is the photon count at pixel i . The spectral response range of the IR camera is $[\lambda_a, \lambda_b]$. The ratio of photon counts can therefore be expanded as

$$\frac{\sum_i \Phi_i}{\sum_i \Phi_{i,ref}} = \frac{\sum_i [f(\lambda_b T_i) - f(\lambda_a T_i)] A \sigma T_i^4}{\sum_i [f(\lambda_b T_{i,ref}) - f(\lambda_a T_{i,ref})] A \sigma T_{i,ref}^4} = \frac{\sum_i [f(\lambda_b T_i) - f(\lambda_a T_i)] T_i^4}{\sum_i [f(\lambda_b T_{i,ref}) - f(\lambda_a T_{i,ref})] T_{i,ref}^4} \tag{E.1}$$

where $f(\lambda T) = \int_0^\lambda E_{\lambda b} d\lambda$, A is the pixel area, and σ is the Stefan-Boltzmann constant. The ratio of radiative heat flux emitted from the experiment is given by

$$\frac{\dot{Q}}{\dot{Q}_{ref}} = \frac{\sum_i A \sigma T_i^4}{\sum_i A \sigma T_{i,ref}^4} = \frac{\sum_i T_i^4}{\sum_i T_{i,ref}^4} \tag{E.2}$$

Considering that in each observation, the temperature of the surface is homogeneous, Eqs. (E.1) and (E.2) can be approximated as

$$\frac{\sum_i \Phi_i}{\sum_i \Phi_{i,ref}} \approx \frac{[f(\lambda_b T_i) - f(\lambda_a T_i)] T^4}{[f(\lambda_b T_{i,ref}) - f(\lambda_a T_{i,ref})] T_{ref}^4} \tag{E.3}$$

$$\frac{\dot{Q}}{\dot{Q}_{ref}} \approx \frac{T^4}{T_{ref}^4} \tag{E.4}$$

The relative error of approximating the radiative heat flux ratio via the ratio of photon counts is obtained by dividing Eqs. (E.3) and (E.4)

$$\frac{\frac{\sum_i \Phi_i}{\sum_i \Phi_{i,ref}}}{\frac{\dot{Q}}{\dot{Q}_{ref}}} = \frac{f(\lambda_b T) - f(\lambda_a T)}{f(\lambda_b T_{ref}) - f(\lambda_a T_{ref})} \tag{E.5}$$

Fixing $T_{ref} = 400^\circ\text{C}$, it is possible to evaluate the relative error of the approximation given in Eq. (E.5) at different representative temperatures T of the experiment. The spectral response range of the camera is $[\lambda_a, \lambda_b] = [1.0 \mu\text{m}, 5.3 \mu\text{m}]$. The relative error made using this approximation grows as the difference in temperature with respect to the reference increases (ΔT), being below 15% for differences as large as 50 K.

Appendix F. Heat loss mechanisms

F.1. Convection

We first consider heat removed by convection above the surface. We assume the surface of the salt is shielded from air flow from the surrounding environment as in the CSPonD design (Gil et al., 2016; Slocum et al., 2011) such that convection losses are due to natural convection. Assuming the surface of the salt and salt-spheres can be treated as heated horizontal plate facing up and that natural convection is turbulent, the Nusselt number is given by

$$\bar{N}u_l = 0.14 Ra_l^{1/3}; 2 \times 10^7 < Ra_l < 3 \times 10^{10} \tag{F.1}$$

where the Rayleigh number Ra_l is given as

$$Ra_l = \frac{\beta \Delta T g l^3}{\nu^2} Pr \tag{F.2}$$

where β is the coefficient of thermal expansion, $\Delta T = T_s - T_e$ is the difference in temperature between the receiver surface temperature T_s and the environment temperature T_e , g is the gravitational acceleration, l is the characteristic length of the receiver, Pr is the Prandtl number, and ν is the kinematic viscosity. The heat transfer coefficient for natural convection \bar{h}_{nc} is then given by

$$\bar{h}_{nc} = \frac{k \bar{N}u_l}{l} = \frac{k}{l} 0.14 \left[\frac{\beta \Delta T g l^3}{\nu^2} Pr \right]^{1/3} = 0.14 k \left[\frac{\beta \Delta T g}{\nu^2} Pr \right]^{1/3} \tag{F.3}$$

where $\bar{h}_{nc} \sim \Delta T^{1/3}$ and does not depend on the characteristic length l . The heat loss by natural convection q_{nc}^{loss} is therefore expressed as

$$q_{nc}^{loss} = \bar{h}_{nc} \Delta T = 0.14 k \left[\frac{\beta \Delta T g}{\nu^2} Pr \right]^{1/3} \Delta T \tag{F.4}$$

F.2. Radiation

The rate of heat loss by thermal radiation is given by

$$q_{rad}^{loss} = \epsilon \sigma T_s^4 \tag{F.5}$$

F.3. Evaporation

The vapor pressures of molten salts are typically quite low, $\approx 0.001\text{bar}$ for chloride salts at 900°C , and the mass losses and corresponding energy losses by evaporation are therefore expected to be small. The fuming rate of chloride salt is given as $200 \text{ g/m}^2/\text{h}$ of exposed surface area of chloride salt at 870°C (ASM, 1991). Vaporization data for molten salts versus temperature is limited and we therefore use the available enthalpy of vaporization of sodium chloride at 800°C (melting point) to estimate the thermal losses by evaporation, given as $\Delta H_{NaCl,800^\circ\text{C}}^{vap} = 45.3 \text{ kcal/mol}$ (Blander, 1964).

$$\Delta H_{vap,NaCl} = 45.3 \frac{\text{kcal}}{\text{mol}} \times \frac{4184 \text{ J}}{1 \text{ kcal}} \times \frac{1}{58.44 \frac{\text{g}}{\text{mol}}} = 3243 \text{ J/g} \tag{F.6}$$

$$\dot{m}_{evap}^{loss} = 200 \frac{\text{g}}{\text{m}^2 \text{ h}} \times \frac{1 \text{ h}}{3600 \text{ s}} = 0.056 \frac{\text{g}}{\text{m}^2 \text{ s}} \tag{F.7}$$

Table F1

Estimated heat loss by convection, radiation, and evaporation and comparison of respective contributions for surfaces at three different temperatures.

T_s (°C)	$Ra_{l=1m} \times 10^{-8}$	\bar{h}_{nc} ($\frac{W}{m^2K}$)	q_{evap}^{loss} ($\frac{kW}{m^2}$, % total)	q_{nc}^{loss} ($\frac{kW}{m^2}$, % total)	q_{rad}^{loss} ($\frac{kW}{m^2}$, % total)	q_{total}^{loss} ($\frac{kW}{m^2}$)
400 °C	39.4	9.17	–	3.4 (24.9%)	10.4 (75.1%)	13
800 °C	81.4	11.68	0.18 (~0)	9.1 (11.9)	66.9 (88.1)	76
1200 °C	123.46	13.42	–	15.8 (6.2)	237.6 (93.8)	253

Table F2

Error introduced in thermal effectiveness of the cover by neglecting natural convection as predicted by the analytical model described in Appendix C.

T_s (°C)	ξ_s with convection	ξ_s without convection	% error in ξ_s without convection
400	54%	49%	–9.3%
800	45%	42%	–6.7%
1200	36%	34%	–5.6%

Table F3

Error introduced in calculated thermal efficiency of an uncovered receiver by neglecting natural convection for solar irradiance $G_s \approx 1$ kW/m².

Solar Concentration	η_c @ 400 °C with convection	η_c @ 400 °C without convection	% error in η_c @ 400 °C without convection
50	0.65	0.71	+9%
100	0.79	0.82	+4%
200	0.87	0.88	+1%

$$q_{evap}^{loss} = \dot{m}_{evap}^{loss} \Delta H_{vap,NaCl} = 0.056 \frac{g}{m^2 s} \times 3243 \frac{J}{g} = 180 \frac{W}{m^2} = 0.18 \frac{kW}{m^2} \tag{F.8}$$

These thermal losses correspond to less than 20% of a natural, unconcentrated solar irradiance $G_s \approx 1 \frac{kW}{m^2}$.

F.4. Magnitude comparison

The estimated heat losses by convection and radiation are reported in Table F1, for surface temperatures $T_s = 400$ °C, 800 °C, and 1200 °C, which correspond to the lowest, intermediate, and highest temperatures investigated in this study, respectively. The estimated evaporation losses at 800 °C are also presented for comparison. The Rayleigh numbers calculated for a characteristic length $l = 1$ m with thermophysical properties of air at the average temperature $\frac{T_s + T_e}{2}$ with $T_e = 25$ °C, are also presented in Table F1 and are shown to be within the range of applicability of Eq. (F.1) Radiation losses are the largest heat losses over the entire temperature range studied. Convection losses are relatively significant at 400 °C and represent 25.7% of the total losses at that temperature. However, this contribution rapidly drops to less than 10% at 800 °C. Evaporation losses are less than 1% of the total heat losses at 800 °C and are therefore assumed to be negligible over the entire temperature range studied.

The thermal effectiveness ξ_s of the cover is expressed as

$$\xi_s = 1 - \frac{\dot{Q}_{cover}^{loss}}{\dot{Q}_{ncover}^{loss}} \tag{F.9}$$

The error introduced by neglecting natural convection in the thermal effectiveness was estimated using the analytical model described in Appendix C. The effectiveness calculated with and without convection for the salt covered with 100 mm-diameter floating spheres, with salt surface temperatures $T_s = 400$ °C, 800 °C, and 1200 °C, and approximate heat transfer coefficient $\bar{h}_{nc} = 10 \frac{W}{m^2 K}$ are reported in Table F2. The estimated error from neglecting convection is largest at the lowest temperature (400 °C) but remains less than 10%. This implies that the cover influences radiation heat losses most significantly. In all cases, the effectiveness of the cover has been under-estimated by neglecting the effects of convection.

The contribution of natural convection losses to the total heat losses, and the corresponding error introduced by neglecting natural convection is most significant at $T_s = 400$ °C, the lowest temperature investigated. Table F3 reports the calculated thermal efficiency of an uncovered surface at $T_s = 400$ °C, for solar irradiance $G_s \approx 1 \frac{kW}{m^2}$, incident on the liquid surface at half-angle $\theta = 0.27^\circ$, and solar concentrations $C = 50, 100,$ and 200 . It can be seen that the thermal efficiency is only over-predicted by 8% for $C = 50$, and the error falls below 1% for solar concentrations above 200. The errors reported in Table F3 will further decrease for increasing temperature. We conclude that for the specific combinations of receiver temperature and solar concentrations relevant to this study, the main quantities of interest, i.e. the thermal effectiveness and thermal efficiency, are estimated with less than 10% error by accounting for radiation losses only.

References

Arpin, K.A., Losego, M.D., Cloud, A.N., Ning, H., Mallek, J., Sergeant, N.P., Zhu, L., Yu, Z., Kalanyan, B., Parsons, G.N., Girolami, G.S., Abelson, J.R., Fan, S., Braun, P.V., 2013. Three-dimensional self-assembled photonic crystals with high temperature stability for thermal emission modification. Nat. Commun. 4, 2630. <https://doi.org/10.1038/ncomms3630>.

ASM, 1991. ASM Handbook. Heat Treating, 10th ed. vol. 4., ASM International. ASTM E490-00a(2014). Standard Solar Constant and Zero Air Mass Solar Spectral Irradiance Tables. ASTM International, West Conshohocken, PA, 2014, www.astm.org, n.d. Atkinson, C., Sansom, C.L., Almond, H.J., Shaw, C.P., 2015. Coatings for concentrating solar systems – a review. Renew. Sustain. Energy Rev. 45, 113–122. <https://doi.org/>

- 10.1016/j.rser.2015.01.015.
- Blander, M., 1964. *Molten Salt Chemistry*. Interscience Publishers, New York.
- Bogaerts, W.F., Lampert, C.M., 1983. Materials for photothermal solar energy conversion. *J. Mater. Sci.* 18, 2847–2875. <https://doi.org/10.1007/BF00700767>.
- Boriskina, S.V., Weinstein, L.A., Tong, J.K., Hsu, W.-C., Chen, G., 2016. Hybrid optical-thermal antennas for enhanced light focusing and local temperature control. *ACS Photon.* 3, 1714–1722. <https://doi.org/10.1021/acsp Photonics.6b00374>.
- Bucci, M., Richenderfer, A., Su, G.Y., McKrell, T., Buongiorno, J., 2016. A mechanistic IR calibration technique for boiling heat transfer investigations. *Int. J. Multiph. Flow* 83, 115–127. <https://doi.org/10.1016/j.ijmultiphaseflow.2016.03.007>.
- Cable, M., 1999. *Mechanization of glass manufacture*. *J. Am. Ceram. Soc.* 82, 1093–1112.
- Calvet, N., Martins, M., Grange, B., Perez, V.G., Belasri, D., Ali, M.T., Armstrong, P.R., 2016. The Masdar Institute Solar Platform: a New Research Facility in the UAE for Development of CSP Components and Thermal Energy Storage Systems. *AIP Conf. Proc.* 1734, 100003. <https://doi.org/10.1063/1.4949191>.
- Codd, D.S., 2011. *Concentrated Solar Power on Demand*. Ph.D. dissertation. Massachusetts Institute of Technology, Cambridge, Massachusetts, USA.
- Cui, F., He, Y., Cheng, Z., Li, Y., 2013. Study on combined heat loss of a dish receiver with quartz glass cover. *Appl. Energy* 112, 690–696. <https://doi.org/10.1016/j.apenergy.2013.01.007>.
- Czarnecki, J.T., 1963. A method of heating swimming pools by solar energy. *Sol. Energy* 7, 3–7. [https://doi.org/10.1016/0038-092X\(63\)90129-4](https://doi.org/10.1016/0038-092X(63)90129-4).
- Drotning, W.D., 1978. Optical properties of solar-absorbing oxide particles suspended in a molten salt heat transfer fluid. *Sol. Energy* 20, 313–319. [https://doi.org/10.1016/0038-092X\(78\)90123-8](https://doi.org/10.1016/0038-092X(78)90123-8).
- Duffie, J.A., Beckman, W.A., 2013. *Solar Engineering of Thermal Processes*. Wiley.
- Dunkle, R.V., 1963. *Thermal radiation characteristics of surfaces*. In: Clark, J.A. (Ed.), *Theory and Fundamental Research in Heat Transfer*. Pergamon Press, New York.
- Epstein, M., Segal, A., Yogeve, A., 1999. A molten salt system with a ground base-integrated solar receiver storage tank. *J. Phys. IV Fr.* 9. <https://doi.org/10.1051/jp4:1999315>.
- Fend, T., Hoffschmidt, B., Pitz-Paal, R., Reutter, O., Rietbrock, P., 2004. Porous materials as open volumetric solar receivers: experimental determination of thermophysical and heat transfer properties. *Energy* 29, 823–833. [https://doi.org/10.1016/S0360-5442\(03\)00188-9](https://doi.org/10.1016/S0360-5442(03)00188-9).
- Fletcher, E.A., 2001. Solarthermal processing: a review. *J. Sol. Energy Eng.* 123, 63–74. <https://doi.org/10.1115/1.1349552>.
- Fletcher, E.A., Moen, R.L., 1977. Hydrogen and oxygen from water. *Science* (80-) 197, 1050–1056. <https://doi.org/10.1126/science.197.4308.1050>.
- Francey, J.L.A., Golding, P., 1981. The optical characteristics of swimming pool covers used for direct solar heating. *Sol. Energy* 26, 259–263. [https://doi.org/10.1016/0038-092X\(81\)90211-5](https://doi.org/10.1016/0038-092X(81)90211-5).
- Francey, J.L.A., Golding, P., Clarke, R., 1980. Low-cost solar heating of community pools using pool covers. *Sol. Energy* 25, 407–416. [https://doi.org/10.1016/0038-092X\(80\)90447-8](https://doi.org/10.1016/0038-092X(80)90447-8).
- Ghasemi, H., Ni, G., Marconnet, A.M., Loomis, J., Yerci, S., Miljkovic, N., Chen, G., 2014. Solar steam generation by heat localization. *Nat. Commun.* 5, 4449. <https://doi.org/10.1038/ncomms5449>.
- Gil, A., Codd, D.S., Zhou, L., Trumper, D., Calvet, N., Slocum, A.H., 2016. Concentrated solar power on demand demonstration: construction and operation of a 25 kW prototype. *AIP Conf. Proc.* 1734. <https://doi.org/10.1063/1.4949115>.
- Karni, J., 2012. *Solar-thermal power generation*. *Annu. Rev. Heat Transf.* 15, 37–92.
- Katsaprakakis, D. Al., 2015. Comparison of swimming pools alternative passive and active heating systems based on renewable energy sources in Southern Europe. *Energy* 81, 738–753. <https://doi.org/10.1016/j.energy.2015.01.019>.
- Kennedy, C.E., 2002. Review of mid-to high-temperature solar selective absorber materials. *National Renewable Energy Lab., Golden, CO (US)*.
- Khullar, V., Tyagi, H., Hordy, N., Otanicar, T.P., Hewakuruppu, Y., Modi, P., Taylor, R.A., 2014. Harvesting solar thermal energy through nanofluid-based volumetric absorption systems. *Int. J. Heat Mass Transf.* 77, 377–384. <https://doi.org/10.1016/j.ijheatmasstransfer.2014.05.023>.
- Kribus, A., Doron, P., Rubin, R., Karni, J., Reuven, R., Duchan, S., Taragan, E., 1999. A multistage solar receiver. *Sol. Energy* 67, 3–11. [https://doi.org/10.1016/S0038-092X\(00\)00056-6](https://doi.org/10.1016/S0038-092X(00)00056-6).
- Lenert, A., Wang, E.N., 2012. Optimization of nanofluid volumetric receivers for solar thermal energy conversion. *Sol. Energy* 86, 253–265. <https://doi.org/10.1016/j.solener.2011.09.029>.
- McMahon, H.O., 1950. Thermal radiation from partially transparent reflecting bodies. *J. Opt. Soc. Am.* 40, 376. <https://doi.org/10.1364/JOSA.40.000376>.
- Menigault, T., Flamant, G., Rivoire, B., 1991. Advanced high-temperature two-slab selective volumetric receiver. *Sol. Energy Mater.* 24, 192–203. [https://doi.org/10.1016/0165-1633\(91\)90059-T](https://doi.org/10.1016/0165-1633(91)90059-T).
- Ni, G., Li, G., Boriskina, S.V., Li, H., Yang, W., Zhang, T., Chen, G., 2016. Steam generation under one sun enabled by a floating structure with thermal concentration. *Nat. Energy* 1, 16126. <https://doi.org/10.1038/nenergy.2016.126>.
- Ni, G., Miljkovic, N., Ghasemi, H., Huang, X., Boriskina, S.V., Lin, C. Te, Wang, J., Xu, Y., Rahman, M.M., Zhang, T.J., Chen, G., 2015. Volumetric solar heating of nanofluids for direct vapor generation. *Nano Energy* 17, 290–301. <https://doi.org/10.1016/j.nanoen.2015.08.021>.
- Otanicar, T.P., Phelan, P.E., Golden, J.S., 2009. Optical properties of liquids for direct absorption solar thermal energy systems. *Sol. Energy* 83, 969–977. <https://doi.org/10.1016/j.solener.2008.12.009>.
- Pacheco, J.E., 2001. Demonstration of solar-generated electricity on demand: the solar two project. *J. Sol. Energy Eng.* 123, 5. <https://doi.org/10.1115/1.1341876>.
- Palik, E.D., 1997. *Handbook of Optical Constants of Solids*. Elsevier.
- Reynolds, D.J., Jance, M.J., Behnia, M., Morrison, G.L., 2004. An experimental and computational study of the heat loss characteristics of a trapezoidal cavity absorber. *Sol. Energy* 76, 229–234. <https://doi.org/10.1016/j.solener.2003.01.001>.
- Romero, M., Buck, R., Pacheco, J.E., 2002. An update on solar central receiver systems, projects, and technologies. *J. Sol. Energy Eng.* 124, 98. <https://doi.org/10.1115/1.1467921>.
- Rowe, D.M., 1981. A high performance thermoelectric solar powered generator. *Appl. Energy* 8, 269–273. [https://doi.org/10.1016/0306-2619\(81\)90023-4](https://doi.org/10.1016/0306-2619(81)90023-4).
- Selvakumar, N., Barshilia, H.C., 2012. Review of physical vapor deposited (PVD) spectrally selective coatings for mid- and high-temperature solar thermal applications. *Sol. Energy Mater. Sol. Cells* 98, 1–23. <https://doi.org/10.1016/j.solmat.2011.10.028>.
- Singh, P.L., Sarviya, R.M., Bhargoria, J.L., 2010. Thermal performance of linear Fresnel reflecting solar concentrator with trapezoidal cavity absorbers. *Appl. Energy* 87, 541–550. <https://doi.org/10.1016/j.apenergy.2009.08.019>.
- Slocum, A.H., Codd, D.S., Buongiorno, J., Forsberg, C., McKrell, T., Nave, J., Papanicolas, C.N., Ghobeity, A., Noone, C.J., Passerini, S., Rojas, F., Mitsos, A., 2011. Concentrated solar power on demand. *Sol. Energy* 85, 1519–1529. <https://doi.org/10.1016/j.solener.2011.04.010>.
- Tetreault-Friend, M., Gray, L.A., Berdibek, S., McKrell, T., Slocum, A.H., 2017a. Optical properties of high temperature molten salt mixtures for volumetrically absorbing solar thermal receiver applications. *Sol. Energy* 153, 238–248. <https://doi.org/10.1016/j.solener.2017.05.054>.
- Tetreault-Friend, M., McKrell, T., Baglietto, E., Gil, A., Slocum, A.H., Calvet, N., Tetreault-Friend, M., McKrell, T., Baglietto, E., Gil, A., Slocum, A.H., Calvet, N., 2017b. Optical property characterization of molten salt mixtures for thermal modeling of volumetrically absorbing solar receiver applications. *AIP Conf. Proc.* 1850. <https://doi.org/10.1063/1.4984419>.
- U.S. Energy Information Administration, 2016. *Electric Power Annual 2015*. Washington, DC.
- Variot, B., Menigault, T., Flamant, G., 1994. Modelling and optimization of a two-slab selective volumetric solar receiver. *Sol. Energy* 53, 359–368. [https://doi.org/10.1016/0038-092X\(94\)90039-6](https://doi.org/10.1016/0038-092X(94)90039-6).
- Weinstein, L., Kraemer, D., McEnaney, K., Chen, G., 2014. Optical cavity for improved performance of solar receivers in solar-thermal systems. *Sol. Energy* 108, 69–79. <https://doi.org/10.1016/j.solener.2014.06.023>.
- Weinstein, L.A., Loomis, J., Bhatia, B., Bierman, D.M., Wang, E.N., Chen, G., 2015. Concentrating Solar Power. *Chem. Rev.* 115, 12797–12838. <https://doi.org/10.1021/acs.chemrev.5b00397>.